Quartz microstructures and crystallographic preferred orientation: Which shear sense do they indicate?

Rüdiger Kilian [a,*], Renée Heilbronner [a], Holger Stünitz [b]

[a] Geological Institute, Department of Environmental Sciences, Basel University, Bernoullistrasse 32, CH-4056 Basel, Switzerland
[b] Department of Geology, University of Tromsø, Dramsveien 201, 9037 Tromsø, Norway

ARTICLE INFO

ABSTRACT

Crystallographic preferred orientation (CPO) and shape fabrics of dynamically recrystallized quartz are currently used as shear sense indicators. We show that the CPO and shape fabric in a polyphase rock do not necessarily indicate the shear sense at the global scale of the shear zone but rather at the local scale of the deforming and recrystallizing quartz aggregates.

In lower amphibolite facies shear zones in the Gran Paradiso metagranodiorite, magmatic quartz grains have recrystallized dynamically by subgrain rotation and grain boundary migration and deform inside a very fine-grained feldspar–mica matrix. The quartz CPO has a peripheral [c]-axis maximum inclined synthetically with the local shear sense. The orientation of the surface fabric is related to the orientation of the [c]-axis maximum and the microscopic shear sense in the quartz aggregate. The geometry of the surface fabric ranges from monoclinic to symmetric depending on the relative contribution of grain boundary migration.

It is inferred that flow partitioning between the quartz aggregates and the matrix controls the local kinematics. CPOs are only reliable shear sense indicators in polyphase rocks if the most highly strained parts are analyzed where spin of the aggregates with respect to the shear zone boundary has ceased.

© 2011 Elsevier Ltd. All rights reserved.

1. Introduction

The objective of this study is to understand the progressive development of quartz fabrics and crystallographic preferred orientations (CPOs) in shear zones. Many insights in CPO development in experimentally or naturally deformed rocks were obtained from studies on monophase material, especially quartzites (e.g. Tullis, 1977; Carreras et al., 1977; Bouchez, 1977; Garcia-Celma, 1983; Schmid and Casey, 1986; Mancktelow, 1987; Law et al., 1990; Heilbronner and Tullis, 2006; Pennacchioni et al., 2010). These studies indicate that asymmetric CPOs can be used as shear sense indicators (e.g. Berthe et al., 1979; Lister and Hobbs, 1980; Simpson, 1980; Behrmann and Platt, 1982; Simpson and Schmid, 1983). In the absence of an internal asymmetry of the [c]-axis pole figure, the interpretation of the shear sense depends on an asymmetry of the pole figure orientation with respect to the chosen kinematic reference frame. Numerical models (Lister et al., 1978; Lister and Hobbs, 1980; Wenk et al., 1989; Jessell and Lister, 1990) demonstrate that the geometry of the CPOs is related to

the applied kinematic framework and pole figures strengthen with increasing strain. The models predict that the CPO rotates with respect to the finite strain ellipse (against the shear sense) as strain increases. CPOs which show this relation have also been reported for natural rocks (e.g. Burg and Laurent, 1978; van Roermund et al., 1979).

In contrast, some quartz CPOs measured in natural shear zones (e.g. Carreras et al., 1977; Simpson, 1980; Garcia Celma, 1983), obtained from numerical models (Etchecopar, 1977; Etchecopar and Vasseur, 1987) or from deformation experiments (Heilbronner and Tullis, 2006) are rotated with respect to the shear zone boundary plane and shear direction, but display no or little rotation with respect to the finite strain.

In order to be able to use the CPO as a reliable shear sense indicator it must be consistent with other shear sense criteria. Oblique foliations (shape fabrics) are easy to recognize and have been related to the deformation mechanism, recrystallization mechanism, and kinematics (Berthe et al., 1979; Means, 1981; Simpson and Schmid, 1983; Lister and Snoke, 1984; Knipe and Law, 1987; Schmid et al., 1987).

We use microstructures in small-scale shear zones which display a strain gradient by a gradually deflected foliation to

---

* Corresponding author. Tel.: +41 61 267 3607.
  E-mail address: ruediger.kilian@unibas.ch (R. Kilian).

reconsider the problem. Progressive CPO development can be observed from initial recrystallization of magmatic quartz grains to fully recrystallized, highly deformed quartz layers which are embedded in a fine-grained feldspar–mica matrix. In this study, the relation of the CPO, shape fabric and shear sense will be discussed with respect to the influence of the recrystallization mechanism, the choice of the reference frame, and the possibility of flow partitioning between quartz aggregates and the feldspar–mica matrix.

2. Geological setting

2.1. Overview

The perminan metagranodiorites of the Gran Paradiso (Fig. 1a) are heterogeneously deformed during the Alpine orogeny (e.g. Dal Piaz et al., 1972; Le Bayon et al., 2006). Meter to kilometer scale low strain domains surrounded by granitic orthogneisses are preserved (Callegari et al., 1969). The metagranitoids have been intensively studied structurally and petrologically (e.g. LeGoff and Ballevre, 1990; Brouwer et al., 2002; Menegon et al., 2006, 2008, Menegon and Pennacchioni, 2010).

The low strain domains host straight, planar small scale shear zones, in regular, equispaced, subhorizontal (and minor subvertical), conjugate arrays (Menegon and Pennacchioni, 2010) (Fig. 1b and c) and several orientation groups of shear zones with a regular spacing have been described. The deformation in the host rock and within the shear zones is assumed to be coeval (Menegon and Pennacchioni, 2010). The metagranodiorite was metamorphosed during (1) an early Alpine event under high pressure conditions at about 500°C–550 °C and 1.0–1.6 GPa and (2) a later event under lower amphibolite facies conditions at about 550 °C and 0.6–0.7 GPa (LeGoff and Ballevre, 1990; Brouwer et al., 2002). The early high pressure event was static and the shear zones formed after peak pressure conditions.

The investigated samples were taken from small scale subhorizontal shear zones in the Piantonetto valley, Lago Teleccio and the Alpe Drosa area (GP9: 32T372881/5038395 GP11/GP12: 32T0371389/5037047) Hand specimens display gradually stronger foliations reflecting strain gradients which can often be observed within one or two thin sections (Fig. 2a and b). Samples GP9 and GP11 are from a medium-grained porphyric metagranodiorite with a quartz content of ~30% (Fig. 2a). GP12 is a microgranitic enclave enclosed in the metagranodiorite (Fig. 2b). The enclave has a biotite–granite composition with a quartz content of ~33% and is devoid of white mica and porphyric K-feldspar. In the field the shear zones from which samples GP11 and GP12 were collected have similar orientations (S136/21,L132/16; S110/19,L114/18) and are from the same outcrop but have opposite shear senses – GP11 top NW, GP12 top ESE.

2.2. Internal structure of the shear zones

In the samples we distinguish a protolith or host rock, a mylonite, and an ultramylonite. The protolith was weakly deformed with a fattening component simultaneously with the shear zones (Menegon and Pennacchioni, 2010). The ultramylonite forms in the most highly strained parts where the foliation is parallel to the shear zone boundary.

The development and progressive rotation of a foliation and the change of shape of mineral aggregates are assumed to result from the strain gradient toward the shear zone center. Least deformed parts of the mylonite show a weak foliation defined by the preferred elongation and orientation of polycrystalline plagioclase and biotite aggregates. Quartz grains of magmatic origin are up to
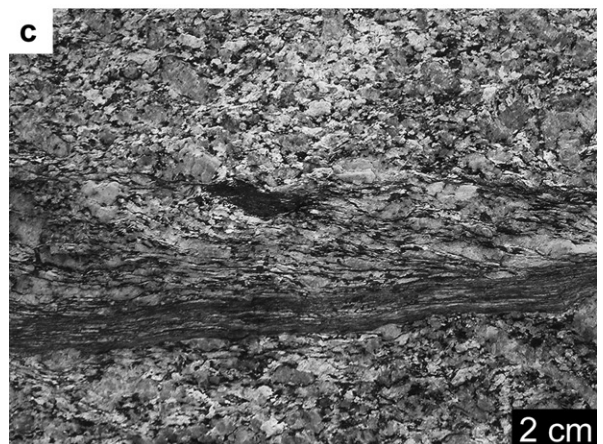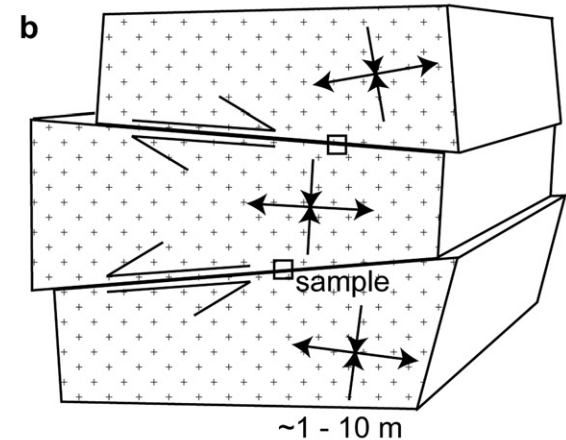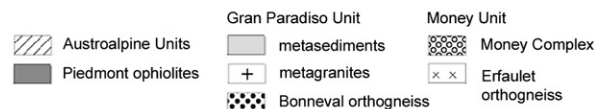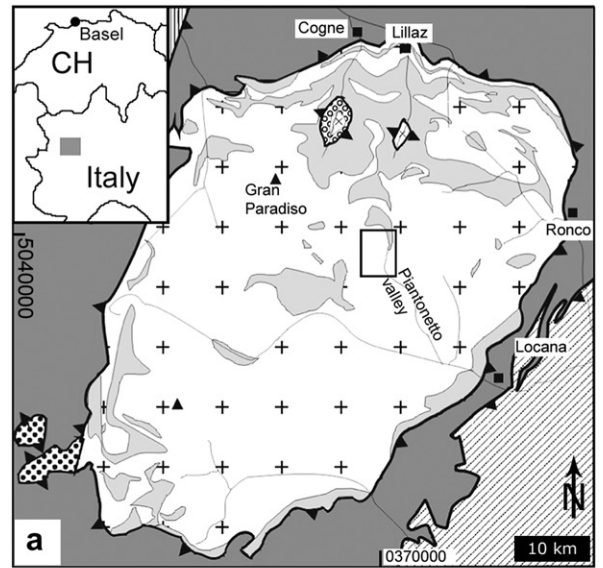
Fig. 1. Geological setting: (a) Geological sketch of the Gran Paradiso nappe (after Kassem, 2005; Menegon and Pennacchioni, 2010). Rectangular area indicates the field area in upper Piantonetto valley. (b) Conceptual sketch showing the subhorizontal shear zones in a low strain domain. (c). Field view of shear zones cutting moderately deformed metagranodiorite. Shear sense is sinistral (top to the west). Area is representative of rectangular inset in (b).
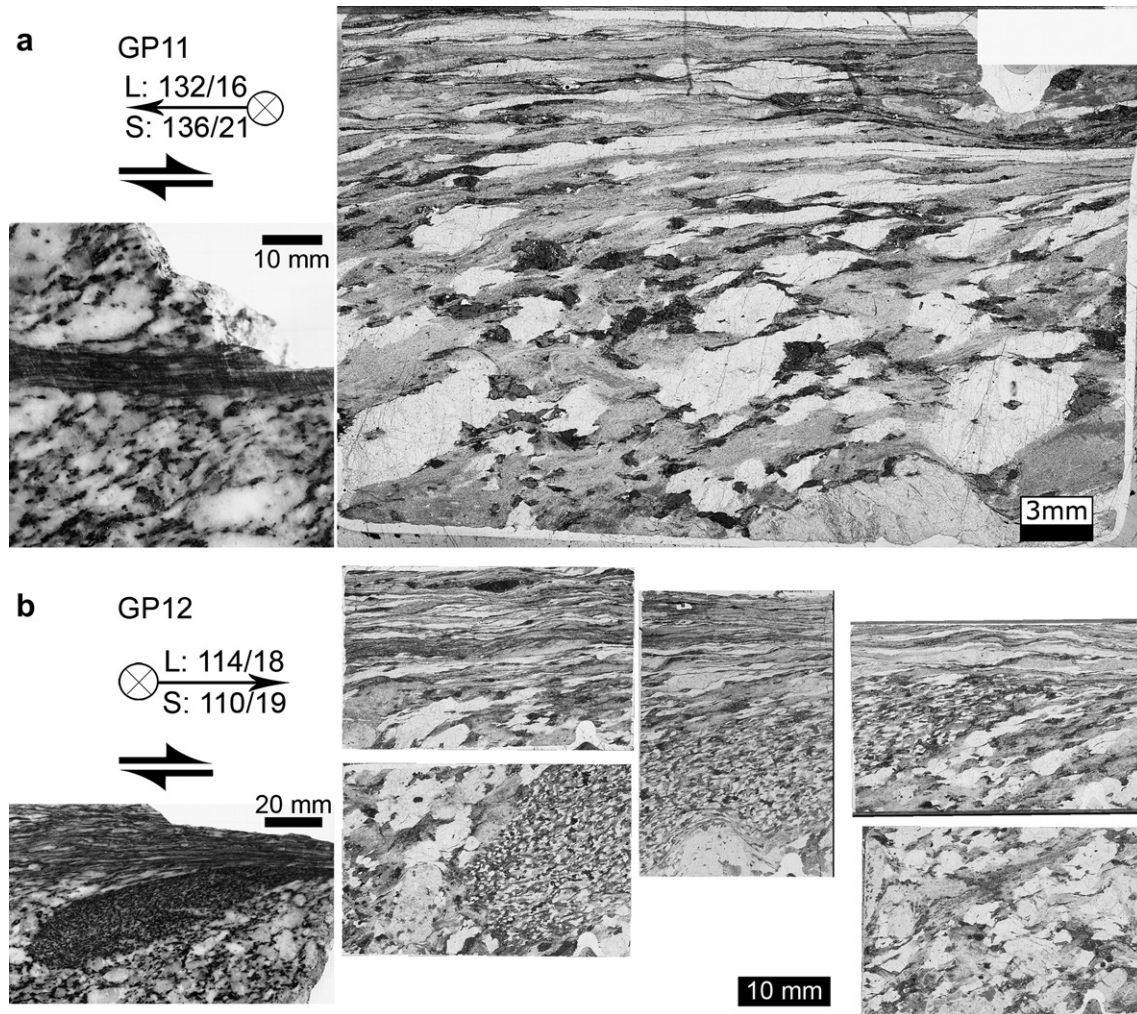
Fig. 2. Samples: Polished rock surface and plane light scans of thin section views of samples GP11 and GP12. GP11 is a medium-grained metagranodiorite. GP12 contains a microgranitic enclave with a smaller size of mineral aggregates. Quartz is white, biotite is brown, fine-grained plagioclase aggregates are gray, K-feldspar is light gray.

10 mm in size in GP11 and ∼1 mm in GP12. At intensely deformed sites, e.g. adjacent to relatively rigid K-feldspar porphyroclasts, magmatic quartz grains begin to dynamically recrystallize. In the more highly strained part of the mylonite, quartz has completely, K-feldspar, biotite have almost completely dynamically recrystallized and former single magmatic quartz grains form polycrystalline aggregates. Recrystallized K-feldspar, plagioclase aggregates and biotite form interconnected layers with a variable degree of phase mixing. Deflection of the foliation clearly indicates the shear sense in both samples (Fig. 2). In the most highly strained parts of the mylonite the quartz aggregates and the phase mixture form parallel layers. In the transition zone to the ultramylonite, the quartz aggregates started to disintegrate and mix with K-feldspar, plagioclase, biotite ± white mica to form a polymineralic fine-grained ultramylonite. This change in microstructure takes place by intergranular dilatancy and K-feldspar and biotite precipitation between quartz grains (Kilian et al., 2011). The ultramylonite is not considered further in this contribution.

2.3. The matrix

In the following, the term matrix is used to describe the partial or complete mixture of all phases except for quartz, i.e. of fine-

grained K-feldspar, biotite, plagioclase, white mica and accessory garnet, epidote, ±clinozoisite.

The plagioclase is of either albite or oligoclase composition, the latter being more common in the highly strained parts. In the undeformed rock, plagioclase occurs in polycrystalline fine-grained aggregates, partially intergrown with variable amounts of white mica or clinozoisite (Fig. 3a). Undeformed plagioclase aggregates are pseudomorphs after undeformed magmatic plagioclase and reach sizes up to 1–10 mm. K-feldspar occurs in the host rock and in the weakly deformed part of the shear zone as perthitic porphyroclasts. Plagioclase aggregates have readily deformed between clasts of K-feldspar or quartz. Large K-feldspar clasts have fractured and subsequently recrystallized. In the more highly strained matrix monomineralic or polymineralic plagioclase − K-feldspar ± mica layers have formed (Fig. 3b). A smaller portion of the matrix plagioclase originates from perthitic exolution or myrmekitic reaction in K-feldspar clasts. The plagioclase grain size in the aggregates remains constant along the strain gradient and is identical to that of the recrystallized K-feldspar with a volumetric mean of 15 μm (Kilian et al., 2011). Magmatic brown biotite is kinked and recrystallized marginally to fine-grained biotite, which forms layers at higher strain. With increasing strain recrystallized biotite grains occur intermixed in the polymineralic layers and pure biotite layers disappear.
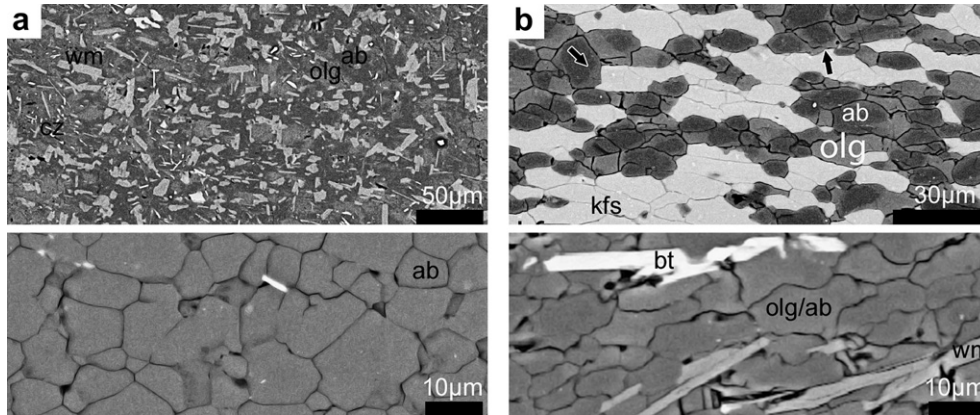
Fig. 3. Matrix microstructures: (a) SEM/BSE micrographs of the undeformed plagioclase matrix with white mica (wm) and clinozoisite (cz) intergrown with albite (ab) and oligoclase (olg). Relatively pure albite aggregates are also common. (b) SEM/BSE micrograph of the deformed matrix composed of polyphase mixture of albite, oligoclase, K-feldspar (kfs), biotite (bt) and white mica (wm). Oligoclase rims growing around albite cores. Deformed plagioclase grains have higher aspect ratios and more lobate shapes than in (a). Images are of sample GP11 except (a) lower picture and (b) lower picture which are from sample GP9.

3. Analytical methods

3.1. Reference frames and definitions

We use the structural *XYZ* coordinate system as the *global reference frame* where *X* is the lineation and transport direction in the shear plane (=parallel to the shear zone boundary), *Z* is the pole of the shear zone boundary and *Y* is the transverse direction (Fig. 4). The *local reference frame XaYZa* is defined by the trace of the aggregate long axis *Xa* (in *XZ*), the pole to *XaY* (=*Za*). *Y* is the same as in the global reference frame (Fig. 4). Angles are counted positive and against the global shear sense from *X* or *Xa*. As a consequence, in a dextral shear zone, positive angles will be counter-clockwise. φ is the angle between an aggregate and *X*, θ is the angle of the [c]-axis pole figure maximum with respect to *X*, and β is the angle between the [c]-axis pole figure maximum and *Xa*. In the most highly strained parts of the shear zone it is impossible to distinguish between the orientation of the shear zone boundary and the quartz aggregate long axis orientation (i.e., $X \approx Xa$). Where quartz aggregates are curved the orientation of the median line has been used. The 'corresponding matrix foliation', Φ, is defined by the mica or plagioclase grain alignment and measured at the same distance from the shear zone boundary as the quartz aggregate (Fig. 4). Directly adjacent to the quartz aggregates the matrix foliation is usually deflected locally, and therefore has not been measured.

3.2. Determination of the crystallographic preferred orientation

The quartz crystallographic preferred orientation (CPO) was analyzed using computer integrated polarization microscopy (CIP) (Heilbronner and Pauli, 1993; Heilbronner, 2000; http://pages. unibas.ch/earth/micro) and EBSD (e.g. Adams, 1993). CIP allows the calculation of [c]-axis orientation images and [c]-axis pole figures. CIP was usually employed for the evaluation of large areas (up to 35 mm^2) because CIP is much less time-consuming than EBSD. EBSD allows the calculation of complete textures. For the CIP analysis, extra thin sections (thickness $\sim$ 20 μm) were used. The input images (1300 $\times$ 1030 pixel) were acquired with a monochromatic IR sensitive camera (Axiocam MRm) on a ZEISS Axioplan microscope. Apart from [c]-axis orientation images, three principal misorientation images were calculated. CIP misorientation images show the angular deviation of the [c]-axis (at each pixel) from a fixed (external) reference direction. The principal misorientation images are calculated with respect to *X,Y,Z*. Using a ZEISS Evo50 SEM, equipped with a Digiview II EBSD camera and OIM software (TSL-Ametek), Euler angles describing the quartz crystal orientations were determined and represented as orientation maps at step sizes of 1–6.75 μm. Pole figures and inverse pole figures were calculated from the raw EBSD data using the MTEX toolbox (Hielscher and Schaeben, 2008). For further details see Kilian et al. (2011).
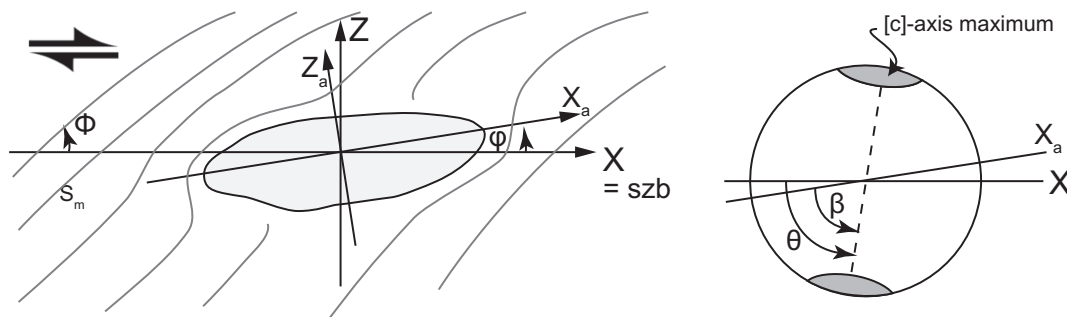
Fig. 4. Definitions of global and local reference frames: The global (shear zone) reference frame is parallel to the shear zone boundary (szb). The local reference frame is parallel to the long axis of the quartz aggregate. φ is the angle of the quartz aggregate long axis with respect to *X*, θ is the angle of the peripheral quartz [c]-axis maximum with respect to the global reference direction *X*, β is the angle of the peripheral quartz [c]-axis maximum with respect to the local reference direction *Xa* ($\theta-\varphi = \beta$). Φ is the angle between *X* and the main foliation (*S*) in the matrix. See text for discussion.

3.3. Grain size analysis

Grain sizes were derived from grain maps which were obtained from CIP-derived misorientation images using the freeware Image SXM (http://www.ImageSXM.org.uk) and the Lazy grain boundaries macro (http://pages.unibas.ch/earth/micro). The orientation difference of [c]-axes across grain boundaries of segmented grains was chosen to be roughly >7.5°. The [c]-axis misorientation angle is always smaller or equal than the real misorientation angle, which is based on the full crystal orientation. Therefore, we may slightly underestimate the recrystallized grain size but we do not miss real

grains with small misorientation angles. A misorientation for a transition from a subgrain to a grain boundary in a certain quartzite is estimated to be around 9° for quartz (Shigematsu et al., 2006). The 2D grain size distributions were obtained by calculating the area equivalent diameters, $dequ = 2 \cdot \sqrt{(area/\pi)}$ of the sectional areas and calculating the corresponding distribution of 3-dimensional spheres using the STRIPSTAR program (Heilbronner and Bruhn, 1998). The 3D grain size distributions thus derived are presented as volume weighted ($v(D)$) or number weighted ($h(D)$) histograms with the arithmetic mean of $v(D)$: $\mu v = \sum(vi(Di) \cdot Di)$ and $h(D)$: $\mu h = \sum(hi(Di) \cdot Di)$.
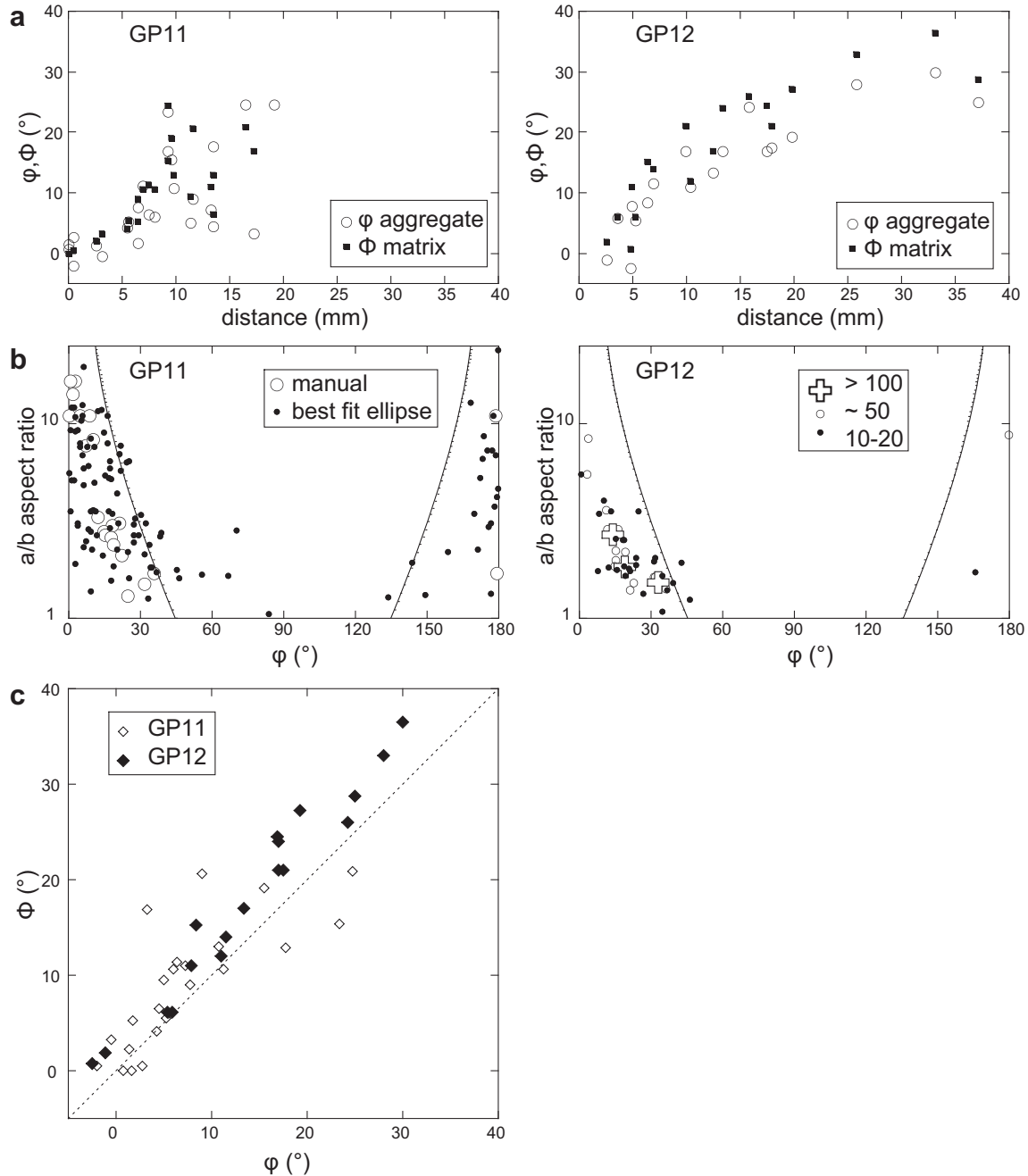
Fig. 5. Shape preferred orientation of quartz aggregates and matrix: (a) Variation of orientation of quartz aggregates and of corresponding matrix foliation orientation with distance from the shear zone center (at 0 mm). (b) Orientation, φ, and aspect ratio of deformed quartz aggregates. The black lines indicate the rotation angle and aspect ratio expected for a passive marker during plane strain simple shear. Data for GP11 is obtained directly from best fit ellipses (black circle) and manually measured large aggregates (open circle). Data for GP12 is obtained from ACF analysis. Numbers denote approximate number of aggregates included in each ACF tile. For discussion see text. (c) Relationship between aggregate orientation φ and corresponding matrix foliation orientation Φ. The dotted line indicates $\varphi = \Phi$.

3.4. Analysis of shape fabrics

The microstructure is described in terms of particle and particle surface orientations using the PAROR (Panozzo, 1983) and SURFOR (Panozzo, 1984) methods. Typical results yield an orientation distribution function (ODF) of long axes of grains (PAROR) and of grain surfaces (SURFOR) presented by length-weighted rose diagrams. The rose diagrams obtained by SURFOR were used to calculate the characteristic shape of the fabric by linking up all surface elements in the order of increasing slope (see Schmid et al., 1987). The projection functions yield the bulk fabric anisotropy, b/a_{bulk} and the bulk preferred orientation of a. b/a_{bulk} is different from the arithmetic mean of axial ratios of individual particles because b/a_{bulk} also depends on the ODF of the particle long axes.

To analyze the shape fabric of entire quartz aggregates, the aspect ratio and long axis orientations were determined on manually produced bitmaps (from photomicrographs) of the aggregates. In the case of the coarse-grained granodiorite, the best fit ellipses were calculated with Image SXM. Where the ellipse fit was poor, angles and axes of the aggregates were measured by hand. In the microgranitic sample GP12 quartz aggregates are small and homogeneously distributed, but display a large spread in shape. Here, autocorrelation functions (ACF) (Heilbronner, 2002) were calculated directly from bitmaps. ACFs with different window sizes (tile size: an ACF tile is the area covered by the autocorrelation function.) were used and aggregate shapes were determined from average ACFs made from tessellations using 3 tiles with >100 aggregates/tile, 15 tiles with ∼50 aggregates/tile, and 26 tiles with 10−20 aggregates/tile. The ACFs were thresholded at a level where the size of the contour corresponds to that of the average aggregate. To determine the orientation and the aspect ratio of the thresholded ACFs, best fit ellipses were used.

The programs STRIPSTAR, PAROR and SURFOR are available at http://pages.unibas.ch/earth/micro/index.html.

4. Results

4.1. Shape and orientation of sheared quartz aggregates

With increasing distance along the strain gradient quartz aggregates progressively elongate and change their long axis orientation toward a smaller angle φ (between X and Xa) together with a rotation of the corresponding matrix foliation (Fig. 5a). Fig. 5b shows the quartz aggregate orientation and aspect ratio measured in samples GP11 and GP12. Sample GP11 has a larger aggregate size and is more heterogeneous. The measured values of a/b and φ do not correspond to the line indicating the expected aspect ratio and ellipse orientation for a passive marker in simple shear and plane strain (strain ellipse) given by

$$a/b = \left[\left(1/\tan^2 \theta \right) + \sqrt{\left(1 + 1/\tan 2\theta^2 \right)} \right]^2$$

for the aspect ratio a/b and the orientation θ of a (after e.g. Ramsay and Huber, 1983). Instead, the quartz aggregates tend to show lower aspect ratios for given angles φ (Fig. 5b). Sample GP12 is more homogeneous, aggregates are smaller, and the ACFs of aggregates shows the same trend as that measured in sample GP11. The angle φ of quartz aggregates in the mylonite is often smaller than the angle of the corresponding matrix foliation (Φ) (Fig. 5c). This relationship is found to be more consistent in sample GP12 than in GP11.

In the most highly strained mylonite, aggregates are aligned parallel to the shear plane and reach aspect ratios >25, separated by matrix layers. The quartz layer thickness is highly variable and can decrease down to the diameter of a single grain (toward the center of the shear zone). Boudinage and pinch-and-swell structures are rare and occur in more heterogeneous parts of the samples, often associated with the development of shear bands.

4.2. Quartz microstructures

In the weakly deformed mylonite the quartz aggregates are composed of magmatic grains rimmed by recrystallized grains. Recrystallized grains decorate the edges of magmatic grains forming core and mantle structures (White, 1976) (Fig. 6a). Relict magmatic quartz grains show a sweeping extinction and are commonly segmented by subgrain boundaries which may form chessboard patterns (Fig. 6a; Baeta and Ashbee, 1969). With increasing strain the fraction of recrystallized grains progressively increases until magmatic grains have been entirely replaced (Fig. 6b and c). Relict magmatic grains from which recrystallized grains originate are referred to as parent grain.

Recrystallized grains generally show a microstructure ranging from interlobate − interlocking to polygonal and square to diamond shaped grains (Fig. 6c−e). Grain boundary segments are straight to curved and frequently meet at angles <120°, although at high magnification triple junctions the angle can be close to 120°. Occasionally, quadruple junctions are present (Fig. 6e). The content of fine-grained solid inclusions is highly variable inside and between different quartz aggregates (Fig. 6e and f).

4.3. Quartz grain size

Sample GP12 contains smaller quartz aggregates which were completely recrystallized at lower strain than in the coarse grained metagranodiorite. The recrystallized grain size in GP12 is approximately the same as in the metagranodiorite GP11. Recrystallized grains have a $\mu v(D)$ of 120 μm and $\mu h(D)$ of 65 μm (Fig. 7a) which remains constant across the shear zone (Fig. 7b). In most cases the grain size has a broad unimodal distribution ranging from approximately 20 to 300 μm with very few grains >200 μm (Fig. 7a). The number weighted distribution is skewed toward smaller grain sizes. The grain size in the single-grain-thick-layers (25−150 μm), which form at high strain, is approximately the same as in the other quartz aggregates. The parent grains and the recrystallized grains contain subgrains. EBSD based subgrain size determinations yield sizes between 20 and 65 μm with a mean size of 40 μm (Kilian et al., 2011).

4.4. Quartz crystallographic preferred orientation (CPO)

Fully recrystallized aggregates contain a strong CPO (Figs. 8 −11a). The dominant CPO type is a peripheral [c]-axis maximum with an external asymmetry with respect to both reference frames, XZ and $XaZa$.

Inverse pole figures with X, Y or Z as reference direction do not show a strong preferred orientation (Fig. 11b). A maximum in the inverse pole figure with respect to the direction perpendicular to the orientation of the [c]-axis maximum (∼160°) is located in the direction corresponding with <a> axes. In the inverse pole figure calculated with respect to 20°, which roughly coincides with the orientation of the maximum surface projection function (15°), directions close to <r>-axes are predominant (Fig. 11b).

The bulk [c]-axis pole figures of the entire shear zones have been calculated from all aggregates, excluding parent grains (Fig. 11c). In GP11 the bulk CPO is similar to the CPOs measured in the most highly strained aggregates but shows an asymmetric spread of [c]-axis orientations along the periphery. The bulk CPO of GP12 also shows a spread along the periphery but a main maximum is less
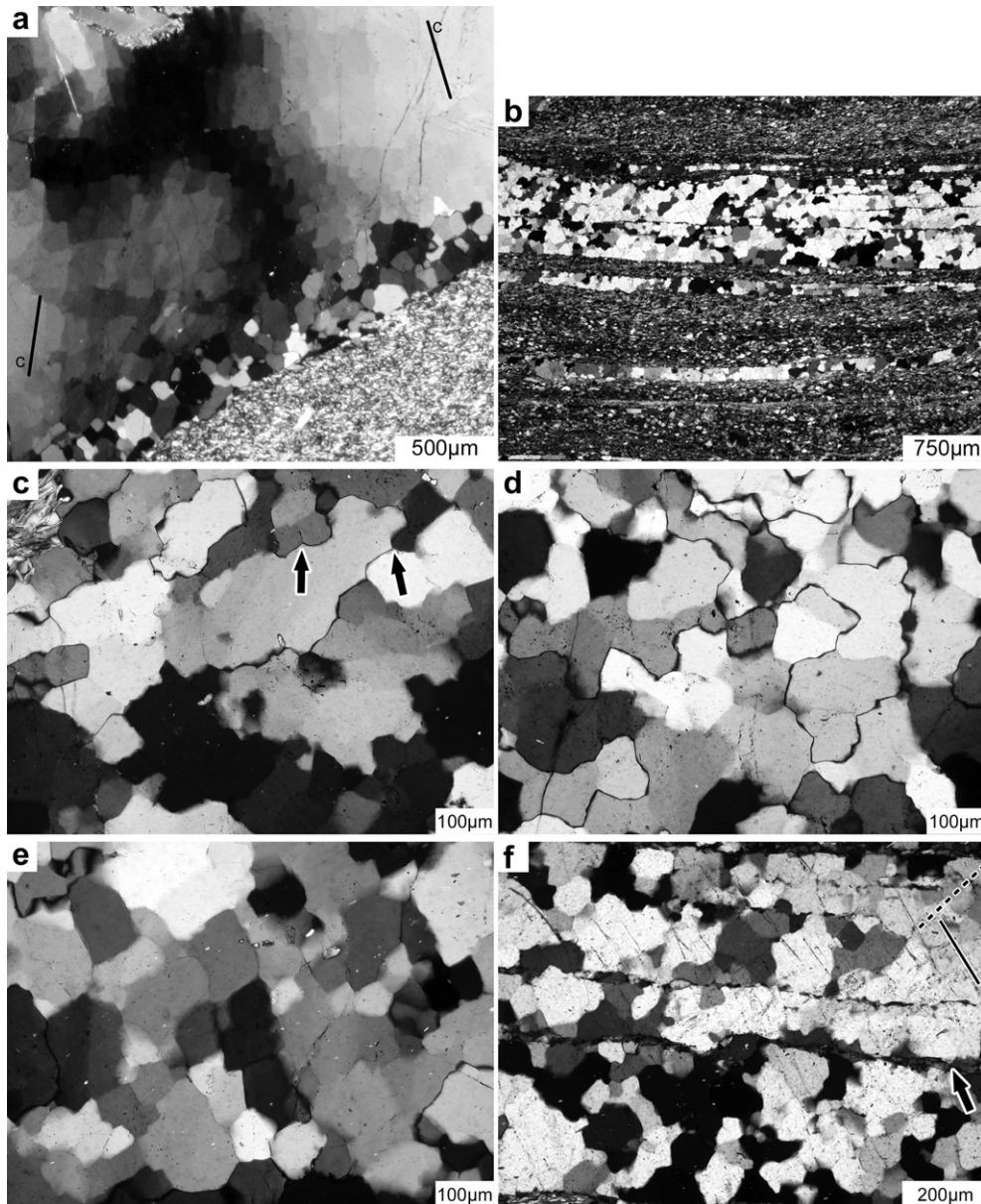
Fig. 6. Quartz microstructures: (a) Parent magmatic grain showing chessboard pattern subgrains and recrystallized grains at the margin. Incipient quartz deformation in the mylonite (GP11). (b) Fully recrystallized quartz aggregate in the highly strained part of the mylonite, forming parallel layers with the matrix (GP9). (c) Grains in a partly recrystallized aggregate in the mylonite. Note grains replaced by grain boundary migration (arrows). (d) Slightly lobate microstructure in fully recrystallized aggregate in the mylonite. Note small-scale straight grain boundary segments (GP11). (e) Diamond-shaped grain boundary alignment in fully recrystallized aggregate in mylonite with low density of second phase particles. Grain boundary segments can align across several grains (GP9). (f) Detail of (b) showing a weak oblique preferred orientation of grain boundaries (stippled line) in quartz aggregate with a high density of second phase particles. Thin, straight inclusion trails with the orientation of the solid line trace late cracks, which crosscut grain boundaries without offset. Some inclusions are aligned along (former) grain boundaries, parallel to the preferred orientation of the grain boundaries and are partly included inside grains (stippled line) (GP9).

pronounced. Bulk [c]-axis pole figures in GP9 are calculated for parallel layers of one and multiple grains thickness and both have the same geometry (Fig. 11d). β is 65° and 70° respectively. The values of the pole figure maxima are 16 and 19, indicating a slightly stronger CPO in the multiple grain thick layers.

4.5. Rotation of the pole figures

The most common CPO in single aggregates is represented by a pole figure with a single peripheral [c]-axis maximum which at high strain show identical angles $\beta = \theta \sim 70°$ which remains stable and does not change with increasing strain, i.e. it is considered to be

a stable end orientation of the pole figure for these mylonites (Figs. 11e and 9). In the case of deflections of the flow plane (e.g. flow around garnet or other rigid inclusions) in the fully recrystallized, layered parts of the shear zone the pole figure rotates with the layer orientation (Fig. 11e). The angle β remains $\sim 70°$ while θ varies up to 30°, depending on the local layer orientation.

The position of the pole figure maximum changes relative to the reference frames (*XYZ*, *XaYZa*) with a decreasing distance to the shear zone center or decreasing φ (Fig. 12a and b). In the highly strained mylonite, where the global and the local reference frame are essentially parallel, the orientation of the pole figures remains constant. The pole figure maximum is consistently inclined with
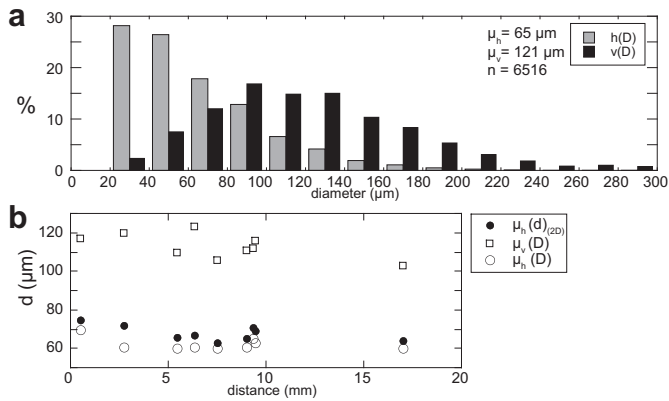
Fig. 7. Grain and subgrain sizes: (a) Size of dynamically recrystallized quartz grains $v(D)$ is volume weighted, $h(D)$ is number weighted. Histogram of all grains of all aggregates analyzed in GP11. (b) Average grain sizes of recrystallized quartz as μv (volume weighted), μh (number weighted) and $\mu h(2D)$ (number weighted 2D) in GP11 obtained from histograms of single aggregates. Distance is in mm from the shear zone center (at 0 mm), same as in Fig. 5a.

the shear sense with respect to the shear zone boundary as well as with respect to the aggregate long axis. At aggregate orientations of $\varphi > 15°$, the CPO maximum is preferentially oriented at $\beta \geq 90°$ with respect to the aggregate long axis (Fig. 12a and b). For smaller angle φ when quartz aggregates become subparallel to the shear zone boundary (X), β decreases below 90°.

In GP12, φ decreases toward the shear zone center and β and θ decrease accordingly but a) two distinct groups are distinguishable (separated at $d \sim 10$ mm or $\varphi \sim 15°$) and b) a smaller relative rotation occurs inside these groups for the angle β ([c]-axis with respect to aggregate) (Fig. 12b). This behavior is less obvious in GP11 which shows a greater range in the distribution of β and θ (Fig. 12a).

The total change of θ is larger than that of β, i.e. the [c]-axis maximum rotates less with respect to the aggregate than with respect to the shear zone boundary, though both rotate with increasing strain synthetically with the local shear sense (Fig. 12a, b and 13). The [c]-axis maximum has been rotated less with respect to the local reference frame when X and Xa are not parallel. In other words, while β decreases by an angle of $\sim 40–50°$ over a distance of 5–15 mm, θ decreases by an angle of 50–70° (Fig. 12a and b).

4.6. Particle and surface fabrics

Fabrics are displayed in the XYZ reference frame. The intensity of the fabric can vary laterally within a single quartz aggregate without any change in CPO geometry, grain size, or visible aggregate stretch. A particle fabric (PAROR) is not pronounced in any of the quartz aggregate but a surface fabric (SURFOR) is more common (Fig. 14).

The anisotropy of the particle fabric is low and the bulk axial ratios b/a_{bulk} are generally larger than 0.80 with an average of b/a_{bulk} of 0.89, which is close to isotropic $(=1)$. The ODF of grain long axes shows a stronger preferred orientation. The ODFs of the surface elements of recrystallized grains typically show either a monoclinic or orthorhombic to symmetric geometry and always have an external asymmetry (Figs. 11a and 13). One maximum aligns preferentially at an angle $(<40°)$ relative to Xa. A second maximum usually develops at a high angle $\sim 70–90°$ to the main maximum (Fig. 14). The most consistent description of their geometry is found with respect to the local reference frame $XaYZa$. The orthorhombic geometries of surface ODF often show two constrictions between the maxima while the monoclinic type has

one constriction. The orientation of the minor or major constriction coincides with the orientation of the [c]-axis maximum. The maximum of the surface ODF is inclined in the same sense the [c]-axis maximum is inclined with respect to Za (e.g. Fig. 14, GP11-1D5a).

4.7. CPO relation to local matrix kinematics and parent grain orientation

Many parent grains show subgrains (Fig. 6a) but a gradual transition from the parent grain crystallographic orientation to the recrystallized grain crystallographic orientation is rare. However, occasionally [c]-axis orientations of recrystallized rims appear as dispersions of the parent grain orientation (Figs. 8 and 9). The relation can be best seen in the site GP11-1D22. The matrix foliation wraps around the and is deflected by a local micro-shear-zone oriented at 145° to X with a synthetic shear sense with respect to the global shear sense (developed between a K-feldspar porphyroclast and the quartz aggregate, lower left). Around the parent grain a thin mantle of recrystallized grains is formed which is oriented at an angle of 70–90° with respect to the matrix around the quartz aggregate. The inclination of the [c]-axis maximum is synthetic with the local shear sense of the matrix around the aggregate. As the matrix wraps around quartz aggregates, there are domains where the c-axes of recrystallized grains shows a gradual increase in misorientation with respect to the parent grain. In that case the CPO of recrystallized grains can be considered as a dispersion of the parent grain orientation. However, for the same clast, other quadrants show a high misorientation of all recrystallized grains with respect to the parent grain and no gradual transition (see Figs. 8 and 9 site GP11-1D22).

4.8. Local and global shear sense

Global shear sense is related to the sense of displacement and was determined by the deflection of the foliation of the shear zone, wherever available by SC′-shear bands, and marker offsets (GP11). Local shear senses were established based on shear sense indicators in the matrix (sigma clasts of mica or plagioclase, drag of mica seams e.g. Simpson and Schmid, 1983; Passchier and Trouw, 1996) which are then compared with the shear senses indicated by the CPO in the quartz aggregates. The interpretation of the latter depends on the chosen reference frame (e.g. Lister and Williams, 1979) and may be ambiguous in the case of weak CPOs (Passchier, 1983).

The CPOs of the Gran Paradiso mylonites have a peripheral [c]-axis maximum inclined synthetically with the local shear sense so that the angle β is $<90°$. The CPO and surface ODF (shape fabric) are in most cases consistent with the local shear sense. Three cases can be distinguished: 1) In the most highly deformed parts, both the CPO and surface ODF show the global shear sense of the shear zone. 2) In the intermediate parts $(\varphi > 15°)$, the CPO and surface ODF of most aggregates show a shear sense contrary to the global shear sense, consistent with the local shear sense in the matrix. 3) Few aggregates with $\varphi \sim 5–15°$ show a shear sense indicated by the CPO consistent with the global shear sense while a weak surface ODF indicates the opposite local shear sense.

The relation of the synthetic and antithetic shear senses with respect to the distance or φ is expressed as a function of $\beta - 90$ in Fig. 12c and d. As the pole figures form peripheral [c]-axes maxima, $\beta - 90$ gives the orientation of the trace of the basal plane of most grains in the aggregate. Below a distance $d \sim 5–10$ mm, which corresponds to an angle $\varphi \sim 10–15°$, aggregates show a synthetic shear sense. Above that distance most aggregates show an antithetic shear sense (Fig. 12c and d). If β is $>90°$ the surface
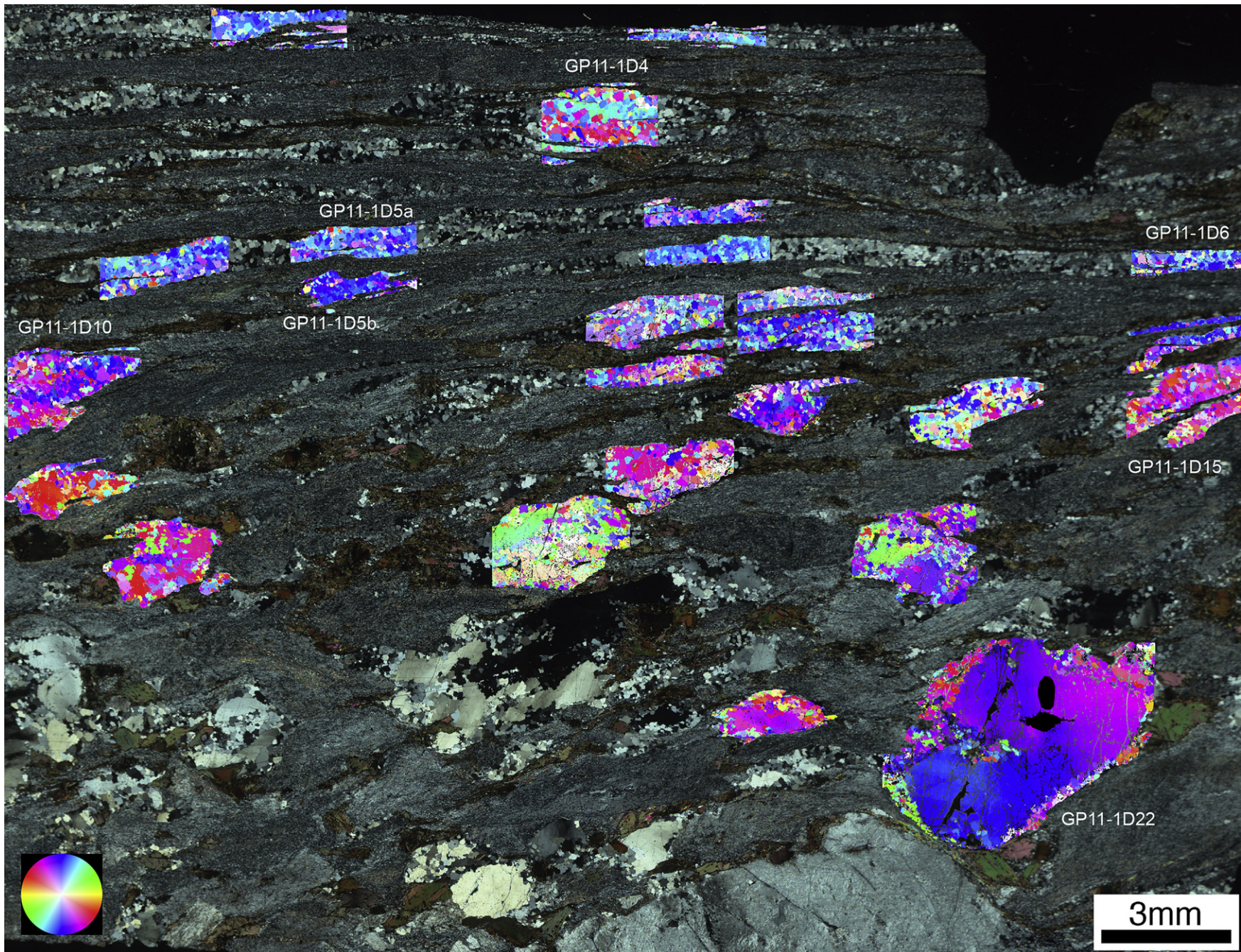
Fig. 8. Overview of sample GP11: Thin section of GP11 (crossed polarizers) showing the sites of CIP-derived [c]-axis orientation images. [c]-axis orientation is color coded according to the look-up table (lower left). Sampling sites further discussed in the text are indicated.
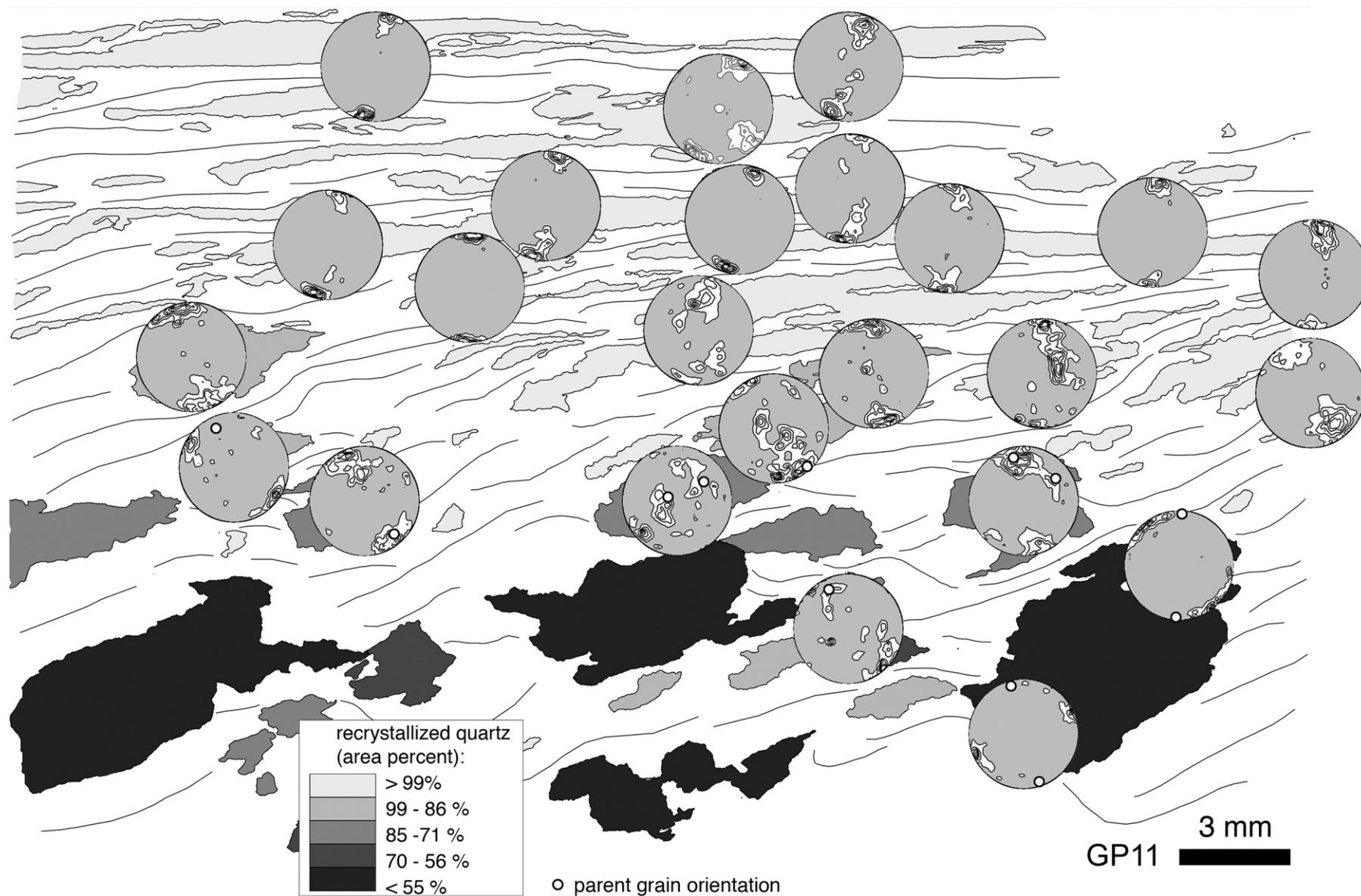
Fig. 9. Overview of sample GP11. Outlines of quartz aggregates and traces of the matrix foliation in sample GP11. Gray values of the quartz aggregates indicate percentage of recrystallized grains. [c]-axis pole figures of recrystallized grains. Contours at 1,2…8 times uniform. White circles in the pole figures indicate the parent grain orientation.

orientation distribution function preferentially shows an asymmetry corresponding to a shear sense opposite to the global shear sense (Fig. 14).

4.9. Relation of pole figure geometry and surface and particle fabrics

The geometry and orientation of surface and particle fabrics seem to be dependent of the pole figure geometry. For an evaluation independent on the differences of local and global shear senses, aggregate GP11-1D4, which is found in the highly strained part of the shear zone, elongated parallel to the shear plane X and Xa (Figs. 15a and 9) is analyzed in more detail. The aggregate consists of two separate domains with contrasting surface fabrics and pole figures. The bulk CPO shows two peripheral maxima oriented at about $\beta = 60°$ and $140°$ (Fig. 15d). The stronger one at $60°$ is consistent with the global shear sense despite being more inclined than the usual pole figures ($\beta \sim 70°$) measured in the high strain part. The surface ODF of each domain shows an asymmetry corresponding with the domain pole figure (Fig. 15b–d). The orientation of the maxima of the bulk surface fabrics of each domain makes an angle to the pole figure maximum of $40°$ in the synthetic domain ($\beta = 60°$) and $-20°$ in the antithetic domain ($\beta = 140°$). The rotation of the pole figure maximum onto the surface fabric maximum shows opposite senses in both domains-clockwise and consistent with the shear sense in the synthetic domain (dextral) and counter-clockwise in the antithetic domain. The surface fabric and CPO of these domains correspond to those aggregates in the mylonite which show a synthetic or antithetic local shear sense, respectively. However in the case of GP11-1D4 there are opposite local shear senses at the domain scale which are different from the local shear sense at the aggregate scale.

In summary, the relationships between the pole figure, the surface fabric, and the shear sense for two different typical aggregates are summarized in Fig. 16a and b. In an aggregate where φ is small, the pole figure maximum is inclined with the shear sense ($\theta = \beta < 90°$). The shear sense is the same as the global shear sense. The characteristic shape has an asymmetry consistent with the shear sense and with the pole figure. In an aggregate with $\varphi > 15°$,

the pole figure maximum is inclined against the global shear sense but with the local shear sense ($\theta > \beta > 90°$). The local shear sense is opposite to the global shear sense. The characteristic shape is again consistent with the local shear sense and the pole figure.

5. Discussion

The discussion will focus on the most important points arising from the observations, namely

(1) That the quartz aggregates are mechanically slightly stronger than the matrix.
(2) That the CPO of recrystallized rims depends on the local kinematics.
(3) That the CPO indicates local shear senses which may deviate from the global shear sense.
(4) That the surface fabric depends on the CPO.

5.1. Deformation of quartz aggregates and matrix

Quartz aggregates deformed in a polycrystalline matrix. The matrix is inferred to have undergone diffusion creep based on the microstructures and the increasing mixture of phases (Kilian et al., 2011). In contrast, quartz aggregates have deformed by dislocation creep, because microstructures indicate dynamic recrystallization, and they have a CPO and a monoclinic surface ODF. The quartz aggregates have convex shapes and the matrix wraps around partly and fully recrystallized aggregates (Figs. 2 and 9). These observations indicate that quartz aggregates are mechanically stronger than the matrix. However, as quartz aggregates neither boudinage nor coalesce to form continuous layers it is inferred that the viscosity of quartz is only somewhat higher than that of the matrix but not much.

Strain theory predicts that the orientation of a particle long axis with respect to the flow plane decreases with increasing aspect ratio (e.g. Passschier, 1987; Schmid and Podladchikov, 2003; Marques et al., 2005; Mulchrone and Walsh, 2006; Mulchrone, 2007). When particle viscosity is higher than the embedding
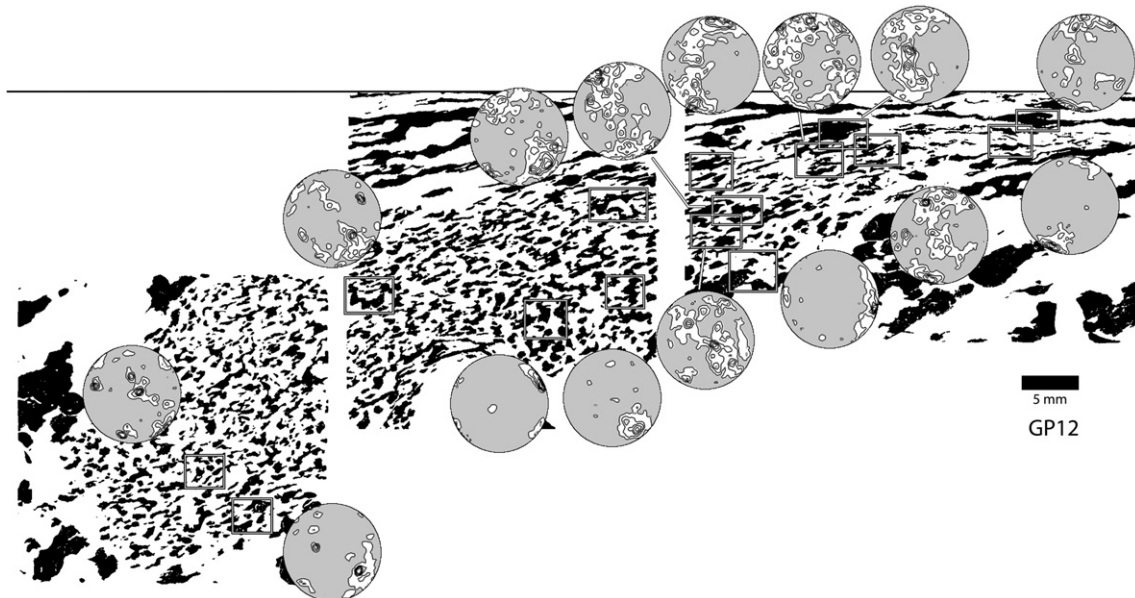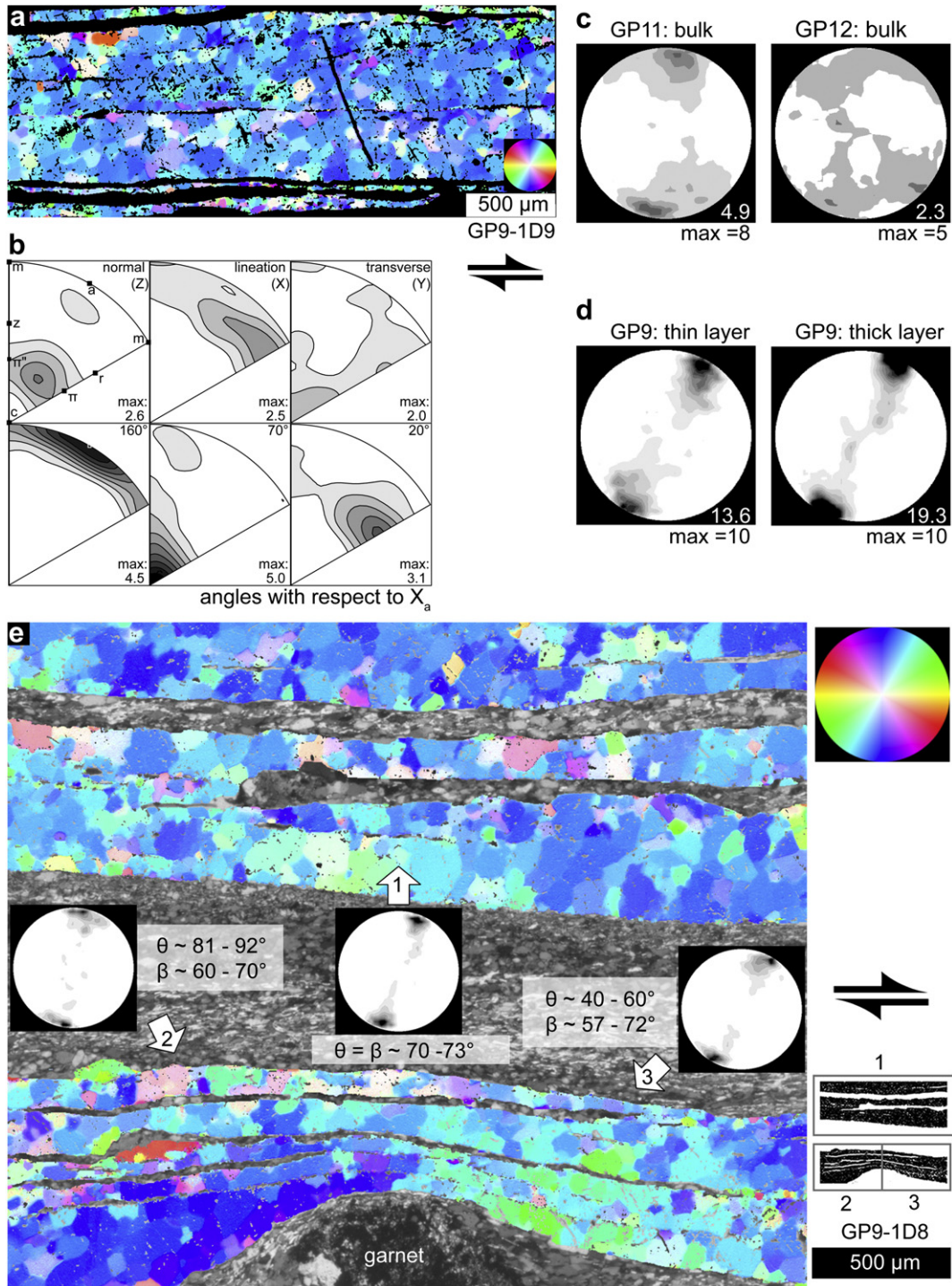

Fig. 10. Overview of sample GP12. Quartz aggregates are black. Percentage of recrystallized grains in the small aggregates in the enclave is ∼ 94% in the left section, and >99% in the right section. [c]-axis pole figures of recrystallized grains. Contours at 1,2…8 times uniform.

Fig. 11. (a) CIP-derived [c]-axis orientation image of a typical quartz aggregate in a highly deformed mylonite (GP9). [c]-axis orientation is color coded according to the look-up table. For pole figure see Fig. 14, GP9-1D9. (b) EBSD derived inverse pole figure of fully recrystallized quartz aggregate comparable to the one shown in (a). Kernel half width 7.5°. Contours at 1,1.5,2…4.5 times uniform distribution. Inverse pole figures were calculated for the reference directions *X,Y,Z* and for the orientation of the [c]-axis maxima (∼70°) and its normal (∼160°) as well as for ∼20° corresponding to the maximum of the surface projection function (angles with respect to *X*). Common crystallographic orientations are indicated in the first inverse pole figure. (c) Bulk pole figures of recrystallized quartz in GP11 and GP12 calculated from all aggregates across the shear zone. Maxima of pole figures is indicated, the displayed maxima are 8 and 5, gray values correspond to 1,2…(5)8 times uniform distribution. (d) Comparison of pole figures obtained from a thin layer (left) and a thick layer (right) in GP9. The thin layer is ∼100 μm (∼1 grain) thick and directly adjacent and parallel to the thick layer which is several grains thick (∼300–600 μm). Total length of measured layers is about 22 mm. The maximum of the pole figure is indicated, the displayed maximum is 10 and gray values correspond to 1,2…10 times uniform distribution. (e) Local rotation of the CPO: [c]-axis orientation image of recrystallized quartz aggregates in a highly strained part of GP9. The layers are parallel to the matrix and change their orientation around a garnet porphyroclast. Note the local orientation deviation of quartz [c]-axes. Pole figures of the upper layers (1) and the left and the right part of the lower layers (2 and 3). The angle *θ* changes with the orientation in the lower layer, *β* remains approximately constant at 70°. CIP-derived [c]-axis orientation image color coded according to look-up table. Shear sense in all figures is dextral.
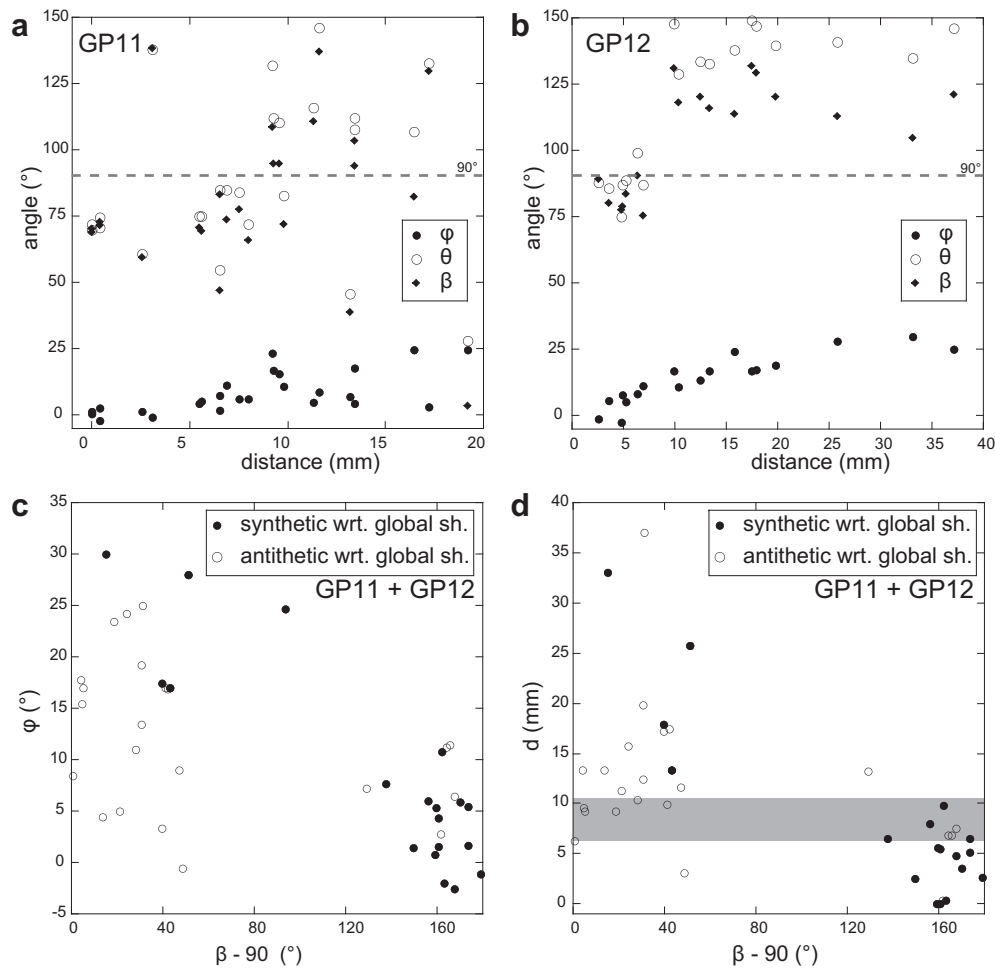
Fig. 12. (a,b) Variation of the angles β, θ and φ for GP11 and GP12 with distance from the shear zone center (=0). (c) Orientation of $\beta - 90$ (trace of the basal plane) with respect to φ. (d) Orientation of $\beta - 90$ (normal to the [c]-axis maximum) relative to the distance from the shear zone center. For (c,d) the different symbols indicate a synthetic or antithetic shear sense in the aggregate. Antithetic and synthetic shear senses are determined from the fabric asymmetry and other available shear sense criteria. Data from both, GP11 and GP12.

matrix, it is expected that the particles rotate faster and change their aspect ratio more slowly than the matrix (e.g. Freeman, 1987; Schmid and Podladchikov, 2003; Mulchrone and Walsh, 2006).

The angle φ of the quartz aggregate is slightly smaller than the angle Φ of the corresponding foliation trace in the matrix, i.e. the quartz aggregate is rotated more than the matrix foliation (Fig. 5c). If bulk simple shear progressive deformation in the shear zone is assumed, it can be interpreted that the quartz aggregates show a higher apparent shear strain than indicated by the corresponding foliation in the matrix. In contrast, the shear strain deduced from the aspect ratio R of the quartz aggregates using $\gamma = (R - 1)/\sqrt{R}$ is lower than that of the corresponding matrix. The values of R and φ in Fig. 5b fall within the field where more viscous particles rotate more and stretch less than expected for a passive marker in progressive simple shear (e.g. Freeman, 1987).

5.2. Recrystallization of parent grains

The presence of a strong CPO and microstructures typical for dynamic recrystallization are indicative for dislocation creep as the deformation mechanism (Figs. 6 and 11). The observed peripheral maximum [c]-axis pole figures are usually interpreted to result from the activity of the basal <a> slip system (e.g. Schmid and Casey, 1986).

Relict magmatic quartz grains have been progressively replaced by recrystallized grains toward the shear zone center (Fig. 9). The

initial recrystallization occurred by progressive subgrain rotation. When the subgrain boundaries become grain boundaries, they become mobile, and grain boundary migration occurs. This process takes place until the relict grain is entirely consumed (White, 1976; Drury and Urai, 1990). The progress of subgrain rotation recrystallization from rim to core is expected to produce a misorientation gradient toward the outer margin of the parent grain, as can occasionally be observed in some porphyroclasts (e.g. Fig. 8, GP11-1D22, lower right). Many parent grains show a high misorientation gradient with respect to the recrystallized grains (Fig. 8). We propose that this situation is the result of grain boundary migration during recrystallization. Recrystallized grains form by subgrain rotation and rotate into orientations suitable to comply with the local kinematics. It was reported that the subgrain size is smaller than the recrystallized grain size and hence grain boundary migration is accompanied by a grain size increase (Kilian et al., 2011) that obliterates the continuous misorientation gradient formed during initial recrystallization. The consumption of non-suitably oriented grains by grains which are oriented in an easy slip orientation has been previously observed in experimentally deformed quartzite (e.g. Heilbronner and Tullis, 2006). The CPO of some recrystallized rims appears in some cases as a broad dispersion of the parent grain crystallographic orientation. This coincidence might be related to crystal plastic deformation of the parent grain preceding recrystallization. However, the orientation of the parent grain finally has little control on the CPO of recrystallized
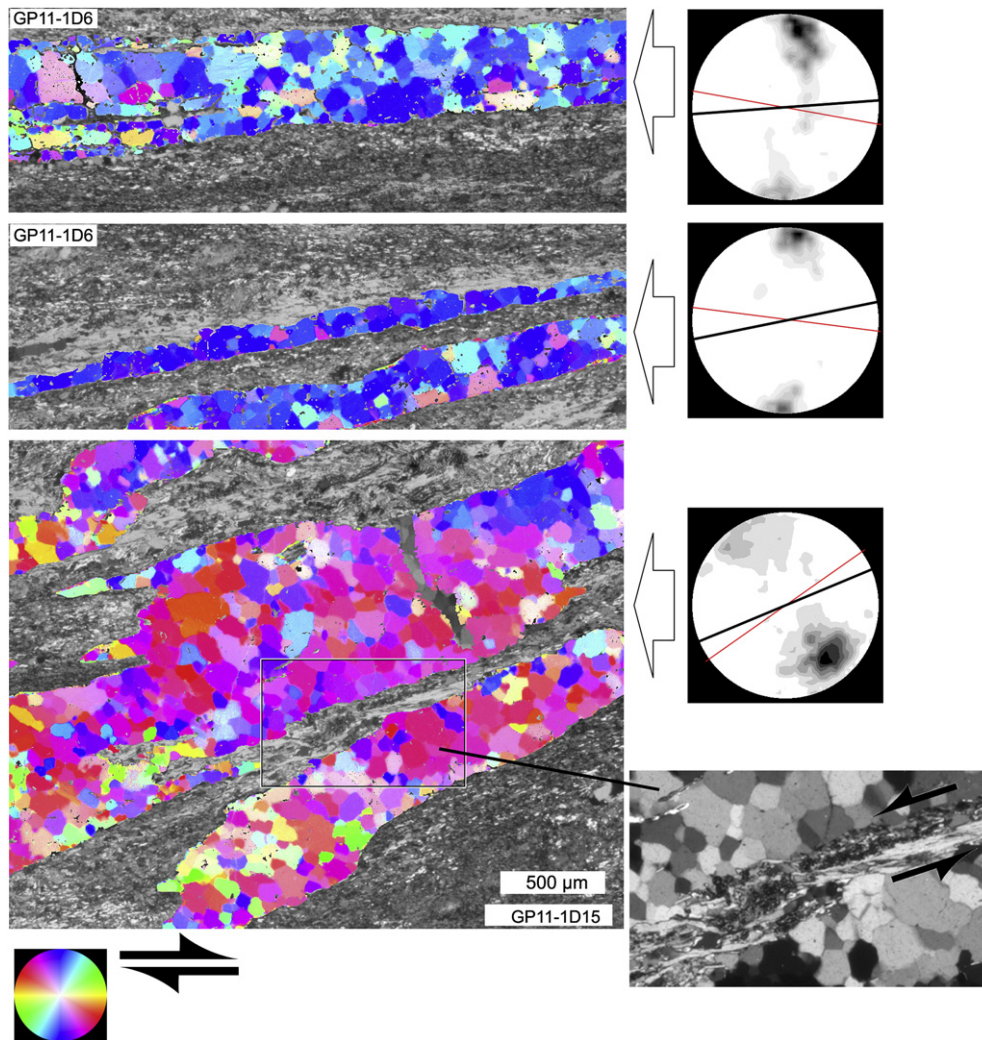
Fig. 13. Re-orientation of the CPO across a strain gradient: [c]-axis orientation images of quartz aggregates progressively rotated into parallelism with the shear zone plane. The red line in the pole figures indicates aggregate long axis, and the black line indicates the normal to the CPO maximum. The indicated shear sense is the (global) shear zone sense. The fabric developed in the lower domains is caused by the local inverse shear sense. Note the mica seams between the lower two quartz aggregates indicating a sinistral shear sense between the layers. See Fig. 13 for details of the CPO and the fabric of GP11-1D15.

aggregates if local strain is high enough (Fig. 8, e.g. site GP11-1D22) and the parent grain orientation is unsuitable to accommodate glide. In the case of only a small difference of parent grain orientation and recrystallized rim, and the parent grain orientations can be regarded as suitable for easy slip, no conclusion can be drawn.

### 5.3. Relation of the CPO and the kinematic framework

[c]-axis pole figures reported in literature are in often either monoclinic or orthorhombic, the former referred to as internally asymmetric. The orthorhombic axes can be inclined with respect to an external reference frame, which is referred to as externally asymmetric. It has been suggested that the asymmetry of a pole figure can be used to infer the shear sense (Etchecopar, 1977; Berthe et al., 1979; Lister and Hobbs, 1980; Simpson, 1980; Behrmann and Platt, 1982; Simpson and Schmid, 1983). According to theoretical CPO models (Lister and Hobbs, 1980) and CPOs measured in well-constrained shear zones (e.g. Behrmann and Platt, 1982; Law, 1986; Schmid and Casey, 1986; Mancktelow, 1987) a monoclinic pole figure geometry serves as a reliable shear sense indicator. We measured CPOs with a peripheral [c]-axis maximum to a weak

straight single girdle or partial straight single girdle, which are mostly orthorhombic. This type of CPO is frequently measured in natural shear zones (e.g. Burg and Laurent, 1978; Simpson, 1980; Garcia-Celma, 1983; Law et al., 1990) as well as obtained from numerical modeling (Etchecopar and Vasseur, 1987; Wenk et al., 1989). The applicability of an orthorhombic single girdle pole figure as a shear sense indicator depends in that case on the reference frame and the chosen CPO model (e.g. Lister and Williams, 1979; Schmid and Casey, 1986).

Existing observations are ambiguous about whether the single girdle orientation rotates with respect to the finite strain axes or the global kinematic framework (e.g. the shear zone boundary plane) or with respect to both. Girdle orientations that remain stable with respect to the global kinematic framework are predicted in numerical models (Lister and Hobbs, 1980; Wenk et al., 1989; Jessell and Lister, 1990) and in some experiments (Bouchez and Duval, 1982; Dell'Angelo and Tullis, 1989) and real shear zones (Burg and Laurent, 1978; Hudleston, 1980; van Roermund et al., 1979). The pole figures in these cases basically rotate with respect to a reference frame defined by the finite strain axes. Other studies indicate that the external asymmetry of the pole figure undergoes
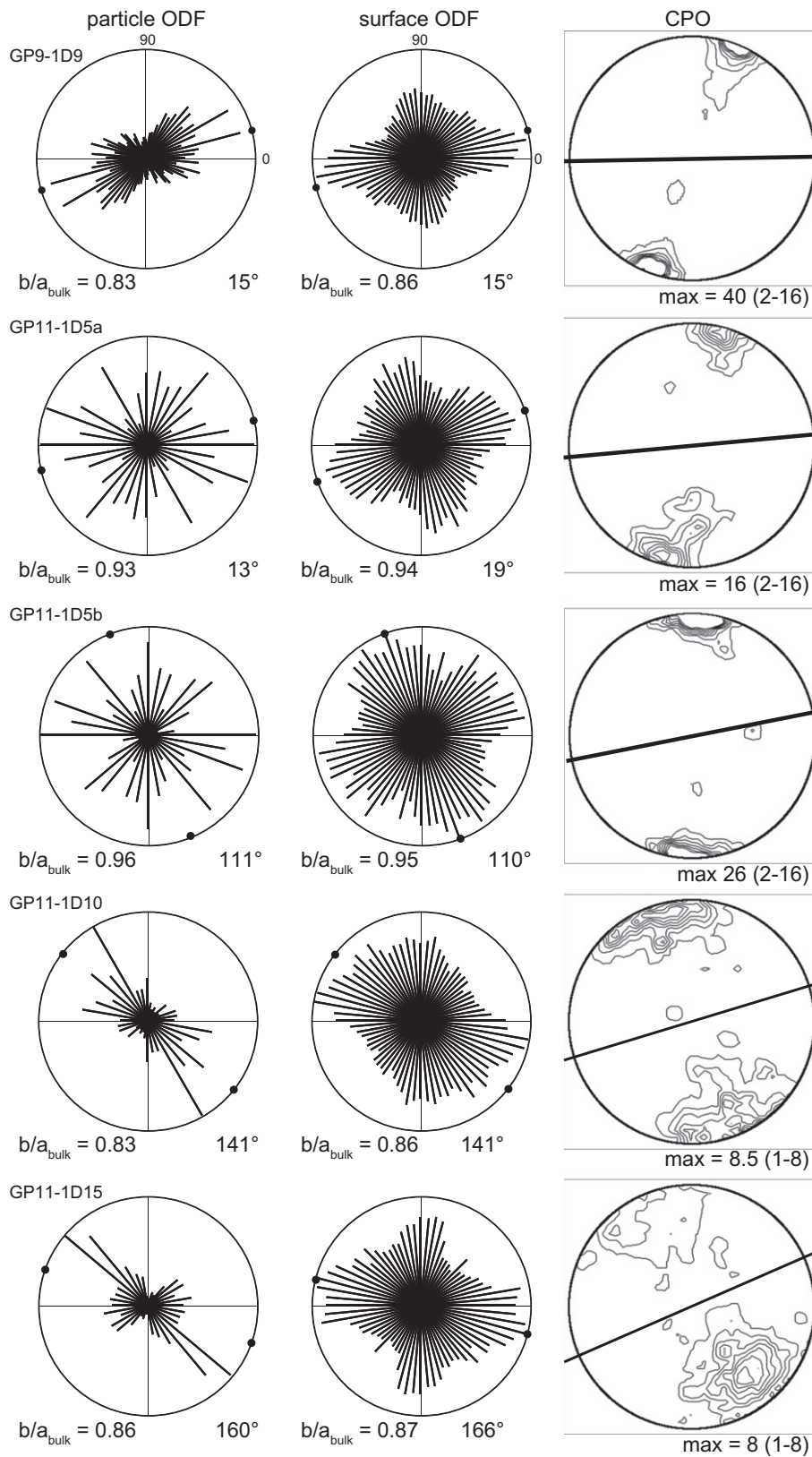
Fig. 14. Shape fabrics and CPO: Particle ODF (PAROR), surface ODF (SURFOR) and [c]-axis pole figures. b/a_{bulk} and orientation of the maximum of the projection function are indicated (in ° and as black dots in the rose diagrams). [c]-axis maxima are indicated, contours are 2,4,…16 and 1,2…8 times uniform distribution. Black line in the pole figure is the aggregate long axis orientation φ. Sampling sites are indicated in Fig. 8, except for GP9-1D9.
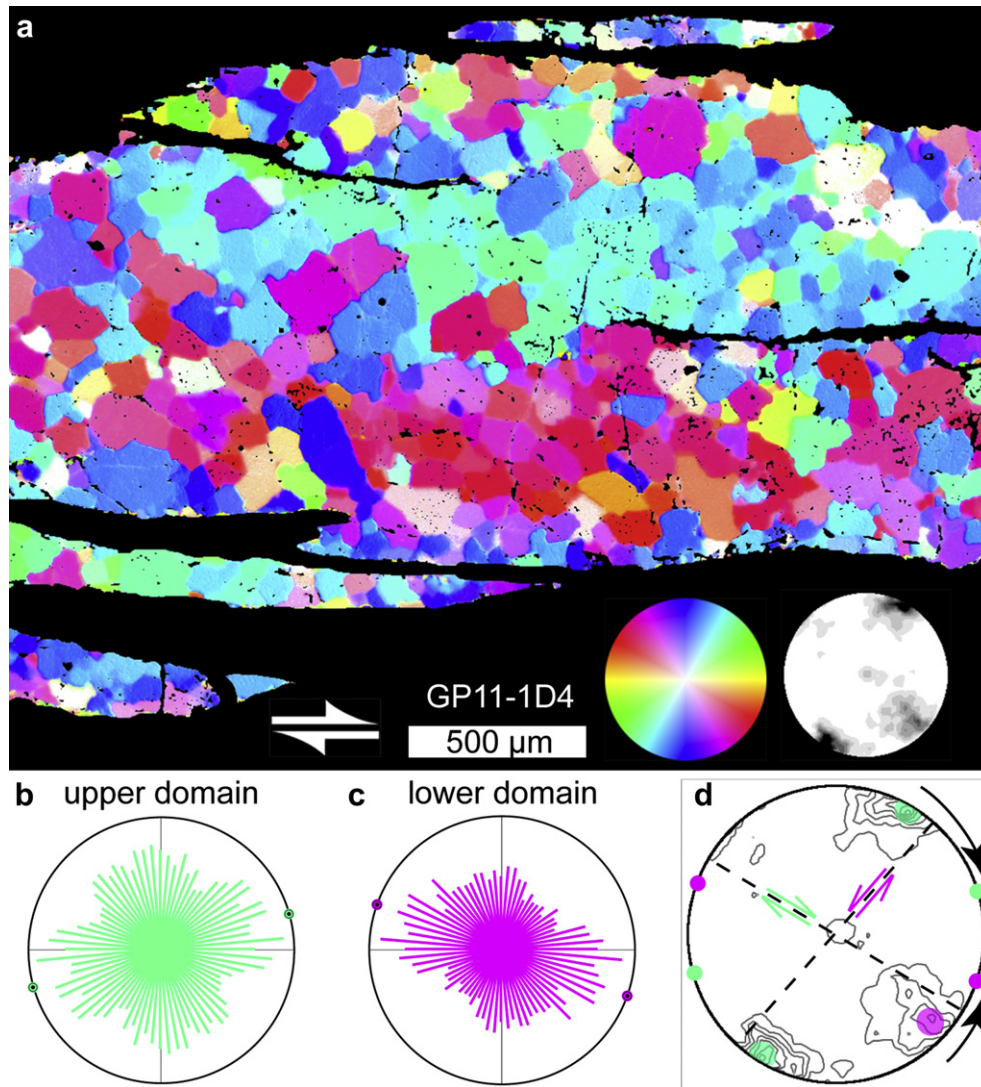
Fig. 15. (a) [c]-axis orientation image of recrystallized quartz aggregate from the highly strained mylonite (GP11-1D4). The (global) shear zone shear sense is dextral, corresponding with [c]-axis orientations showing blue-greenish colors. Note the oblique fabric in the red domain, inclined against the global and main local shear sense. (b,c) Surface orientation distribution functions of the upper and lower domain. (d) Pole figure showing the maxima of each domain, the plane perpendicular to the maxima (inferred basal plane, stippled line), the maxima of the surface projection function (solid dots). The rotation of the "surface" maxima relative to the pole figure maxima is in both domains synthetic with respect to the inferred shear sense on the basal plane. The shear sense is synthetic with the global shear sense in the upper domain and antithetic in the lower domain.

only minor rotation with respect to the orientation of the inferred finite strain axes (Carreras et al., 1977; Simpson, 1980; Garcia-Celma, 1983; Schmid and Casey, 1986; Etchecopar and Vasseur, 1987; Heilbronner and Tullis, 2006) and major rotation occurs with respect to the shear zone boundary plane with increasing strain. At high strain single girdle or peripheral maxima tend to rotate synthetically with the shear sense resulting in a stable orientation that can no longer be simply related to finite strain (e.g. Schmid and Casey, 1986). Some of the differences in apparent shear sense can be related to flow partitioning between the quartz and the host rock (e.g. Carreras et al., 1977; Lister and Williams, 1979), but it is not clear whether flow partitioning occurs in pure quartz rocks (e.g. Heilbronner and Tullis, 2006).

Quartz pole figures measured in the Gran Paradiso mylonites are in most cases orthorhombic with a single peripheral [c]-axis maximum and show major rotations with respect to the shear zone reference frame (XYZ) and minor ones with respect to the local reference frames ($XaYZa$) (e.g. Figs. 12 and 14). We observe that the

[c]-axis maximum is inclined with the local shear sense and that the CPO reaches a stable position ($\theta \sim \beta \sim 70°$) as soon as aggregate rotation ceases in the most highly strained parts. The stable orientation of the CPO maxima does not change as long as layers remain parallel to the shear zone boundary (Fig. 11). The inclination of $\beta \sim 70°$ or roughly $\sim 110°$ with respect to the local reference frame is also readily attained if strain is locally large enough (Fig. 12a and b). From these observations we conclude that the CPO develops in relationship to a local kinematic framework but does not develop in a relationship to a fixed global kinematic framework (CPO rotates with respect to the shear zone boundary) and not in a relationship to the orientation of the finite strain axes of the entire shear zone (CPO deviates around clasts and reaches a stable, strain independent orientation).

The rotation of the local kinematic framework with respect to the global kinematic reference frame causes an apparent discrepancy with predictions of numerical models (Lister and Hobbs, 1980; Etchecopar and Vasseur, 1987; Wenk et al., 1989; Jessell and Lister,
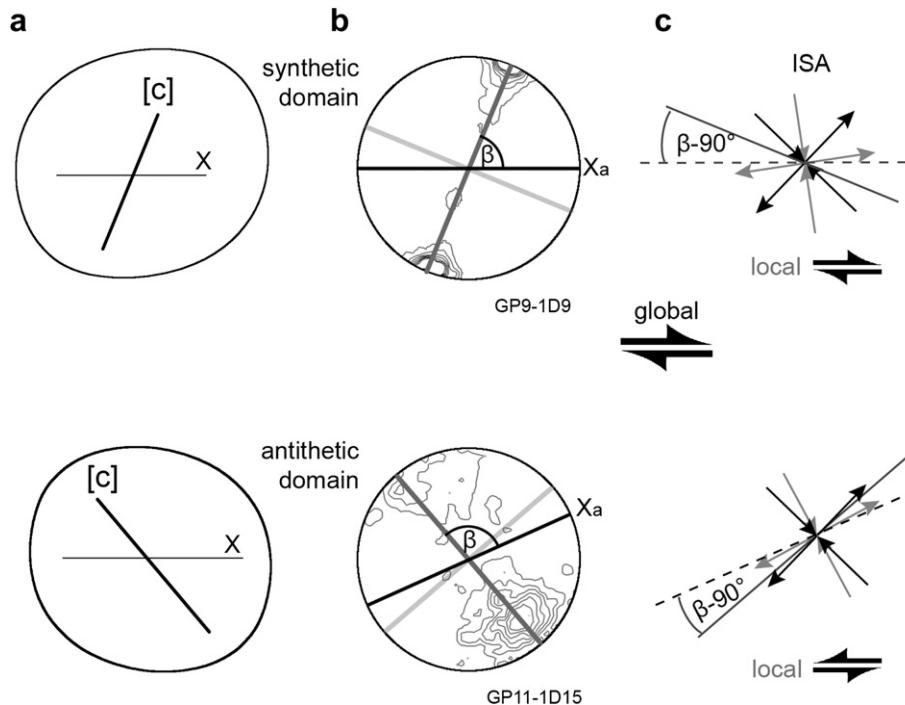
Fig. 16. Summary of the surface fabrics and CPO analysis showing (a) the characteristic grain shape (derived from the SURFOR orientation distribution function) with a trace of the [c]-axis pole figure maximum of recrystallized grains, (b) The pole figure and (c) Two hypothetical instantaneous stretching axes (ISA). The gray line in the pole figure indicates the trace of the plane normal to the [c]-axis maximum (i.e. most basal planes of quartz crystals in the aggregate), the black line the aggregate angle φ between X and Xa (see Figs. 11a and 13 for details of the fabric). The top row is obtained from an aggregate parallel to the shear plane with a typical CPO and surface fabric. The bottom row is obtained from an aggregate inclined to the shear plane, showing an antithetically rotated CPO and surface fabric maximum. The trace of the basal plane ($\beta - 90$) is antithetically rotated (with respect to global shear sense) with respect to the aggregate orientation (gray line) of GP11-1D15. Two sets of inferred ISA are shown, one stable (assuming simple shear) to the global reference frame (black) which is always at 45° with respect to the shear zone boundary and one rotated with the shear sense about an angle smaller than the aggregate rotation (gray). See text for discussion.

1990) and experimental or natural shear zones (Burg and Laurent, 1978; van Roermund et al., 1979; Bouchez and Duval, 1982). This discrepancy can be explained − at least in part − by pointing out that in some of those studies where the developing pole figures rotate with respect to the shear zone boundary (e.g. Carreras et al., 1977; Simpson, 1980; Garcia Celma, 1983) either the kinematic framework rotated, too, or the kinematic vorticity number increased with progressing deformation. Schmid and Casey (1986) suggest that a rotation of a single girdle may result from an increasing non-coaxiality (increasing kinematic vorticity number) or from increasing strain by progressive simple shear until a stable position is reached. Heilbronner and Tullis (2006) observed a major rotation of the pole figure with respect to the shear zone boundary with increasing strain in shear experiments but steady state presumably was not attained.

Opposite external CPO asymmetries found around quartz aggregates have been interpreted as opposite shear senses caused by strain partitioning around porphyroclasts (e.g. Garcia-Celma, 1983; Jerabek et al., 2007). In the present work the contrasting CPO asymmetries in the recrystallized rims of some of the parent grains are interpreted in such a way that the local kinematic framework is heterogeneous around the aggregate and controls the final CPO in the rim. The changes of the local kinematic framework (Figs. 8 and 9, e.g. site GP11-1D22, Fig. 15) result from the flow behavior of the matrix around the quartz aggregates and possibly spin of the aggregate with respect to the shear zone boundary.

The population of angles β yields a gap around 90°−100° which indicates an instability of a [c]-axis orientation at $\beta \sim 90°$ (Fig. 12a and b). Recrystallized grains readily rotate into orientations suitable for flow in response to matrix kinematics even in the least strained

parts of the shear zone if local strain of the rim is high enough. The angles of $\beta > 90°$ for aggregate orientations with $\varphi > 15$ are related with local antithetic shear senses (Figs. 12c,d and 13). Consequently, a rotation of the pole figure with the local shear sense out of the 90° orientation can potentially explain the distributions of angles β. These relations generally show less scatter in sample GP12 which is more homogenous than sample GP11.

It is concluded that the CPO of the recrystallized rim depends mainly on the local kinematic framework around the aggregates. The CPO readily adjusts with increasing strain in the aggregate toward a stable position with respect to the local kinematic framework but this local kinematic framework changes inside the shear zone as the aggregates rotate with increasing finite strain. The re-orientation of the local kinematic framework competes with the strain-dependent rotation of the CPO toward a stable orientation − individual CPOs are the results of these competing processes.

5.4. Relationship between CPO and shape fabric

Asymmetric particle and surface ODFs, also recognized as oblique grain shape fabrics or oblique foliations, have been used to infer the shear sense (e.g. Berthe et al., 1979; Simpson and Schmid, 1983; Lister and Snoke, 1984; Knipe and Law, 1987). We observe that the asymmetry of the surface ODF generally coincides with the orientation of the [c]-axis pole figure maximum (Fig. 14). The particle fabrics usually are weak, but if there is a preferred orientation, all the pole figures show a steeper inclination than the particle and surface ODFs with respect to Xa (e.g. GP11-1D15 in Figs. 14 and 15d). Independent whether the surface ODFs geometry (symmetric or monocline), all surface ODFs show a small constriction which

coincides with the orientation of the [c]-axis maximum (Figs. 14 and 15). This contrasts with observations in dynamically recrystallized quartzites, where the submaximum of the surface orientation distribution function is interpreted to coincide with the pole figure maximum (Stunitz, 1991).

The relation of the surface ODF and the CPO found in aggregate GP11-1D4 suggests that the surface ODF depends on the [c]-axis orientation rather than on the kinematic framework or shear sense (Fig. 15). The aggregate is situated in the highly strained part of the mylonite (Fig. 8) and shows two [c]-axis orientation domains, one of which is inclined against the shear sense and both with a corresponding surface fabric (Fig. 15). However, in that case there is no reason to assume two opposite local shear senses at the aggregate scale rather than at the domain scale. Therefore, the asymmetry of the surface ODF cannot be related to the macroscopic shear sense but it is proposed that it is rather related to the microscopic shear sense related to deformation and recrystallization of individual grains in each domain. Similar observations in domainal microstructures have been interpreted as being caused by an antithetic shear using a similar slip system in combination with grain boundary sliding and migration (Pauli et al., 1996).

Two main processes can be considered to influence the surface fabric of grain boundaries during dislocation creep: 1) subgrain rotation recrystallization and 2) grain boundary migration.

5.4.1. Process 1: subgrain rotation recrystallization

Subgrain rotation recrystallization produces boundary orientations depending on the slip system and the dislocation type (Baeta and Ashbee, 1969; Trepied et al., 1980). Most observed subgrain boundaries in the quartz aggregates are preferentially parallel to a trace of a prism plane and can be interpreted as tilt boundaries of basal edge dislocations with Burgers vector <a> (e.g. Trepied et al., 1980). Grain boundaries are therefore required to rotate relative to the [c]-axis to meet the observed relation. A rotation of the grain boundary in the sense of a rotation of a material plane with respect to the crystal orientation requires that the grain deforms internally. Nevertheless, the grains in the Gran Paradiso metagranodiorite have relatively equant shapes.

The measured single maximum pole figures show little spread and are not consistent with large lattice rotations in individual grains unless there is substantial compensation by the spin of grains in the opposite direction. A potential explanation can be provided by a combination of grain rotation (spin) and an internal opposite [c]-axis rotation (e.g. Pauli et al., 1996). The spin of grains implies grain-scale strain partitioning because a compensating mechanism is required if there is only one dominant slip system involved (Mancktelow, 1987; Schmid, 1994; Pauli et al., 1996). Therefore, if subgrain rotation recrystallization is the process responsible for the generation of grain boundaries, slip on the basal <a> slip system has to be accompanied by an unidentified slip system or grain boundary sliding to explain the CPO-monoclinic surface ODF relation.

5.4.2. Process 2: grain boundary migration

The driving potential for grain boundary migration is a difference in strain energy (volume energy) (e.g. Poirier and Guillope, 1979; Guillope and Poirier, 1980) which in itself should lead to an isotropic fabric.

However, in many situations where grain boundary migration is involved in dynamical recrystallization – like in our example – anisotropic fabrics have been reported (e.g. Lister and Snoke, 1984; Knipe and Law, 1987). We observe a minor constriction in the surface ODF in the position of the [c]-axis maximum, which suggests that grain boundaries preferentially do not contain the trace of the [c]-axis. Kruhl and Peternell (2002) described a preferential development of rhombohedral planes at amphibolite facies conditions and Kuntcheva et al. (2006) report a preponderance of rhombohedral and high index planes and a preferential development of boundaries at around 25–50° to the [c]-axis in dynamically recrystallized quartz from amphibolite facies gneisses. As long as the [c]-axis lies in the plane of observation, the trace of {r}-planes cannot be parallel to the trace of the [c]-axis. The maximum of <r>- poles in inverse pole figures plotted with respect to the direction of the surface ODF maximum (Fig. 11b) could explain the constrictions in the surface ODF at the [c]-axis maximum position if {r}-planes are developed as grain boundaries.

Various explanations have been suggested for the origin of anisotropic fabrics formed during grain boundary migration. Anisotropic material properties such as anisotropic surface energy could potentially cause the preferred orientation of certain boundaries during grain boundary migration (Kuntcheva et al., 2006). The contribution of surface energy to the driving potential of grain boundary migration during dynamic recrystallization is dependent on grain size and differential stress (Poirier and Guillope, 1979; Guillope and Poirier, 1980). With regards to the large grains size in the Gran Paradiso mylonite, it is questionable whether surface energy may provide a significant contribution to grain growth (Platt and Behr, 2011). So it remains open what drives the grain size increase from subgrain size to recrystallized grain size and therefore if anisotropic surface fabrics can be related to a crystallographically related effect.

5.4.3. Comparison of both processes: subgrain rotation–grain boundary migration

The strength of the surface fabric measured by b/a_{bulk} is variable and the microstructure and the type of surface fabric varies considerably (e.g. Fig. 6d–f and 14) even within one highly stretched quartz aggregate. This variation can be roughly correlated with the amount of second phase particles (Fig. 6e and f) and microstructures indicative of pinning. Pinning and therefore the grain boundary mobility are related to the amount and distribution of second phase particles (e.g. Olgaard and Evans, 1986). It is suggested that the heterogeneous distribution of second phase particles resulted in a heterogeneous grain boundary mobility that can account for the differences in the observed microstructures and surface fabrics.

The contribution of two processes is envisaged to act concurrently to produce a surface fabric: migration and rotation of grain boundaries. At low grain boundary velocity, locked or slowly migrating grain boundaries behave as material planes and rotate as the grain deforms internally which leads, – assuming the formation of new grain boundaries by subgrain rotation recrystallization – to a monoclinic surface ODF. Conversely, at high grain boundary velocity strain-dependent grain boundary rotation is less important than grain boundary migration for developing surface ODFs. Such an interpretation complies with the observations of strong monoclinic surface ODFs in inclusion rich parts and more orthorhombic to symmetric surface ODFs in inclusion poor parts of quartz aggregates (Fig. 6e and f).

5.5. Flow partitioning

As outlined earlier the aspect ratio and φ-data of the quartz aggregates and the absence of coalescence supports the interpretation that they deformed as more viscous objects in a less viscous matrix. The apparent flattening (Menegon and Pennacchioni, 2010) of quartz aggregates can be attributed to a higher rate of rotation (spin) and a lower strain rate in the quartz aggregates than in the matrix. However, the previously noted reversal of the local shear sense requires an explanation. In the case where a more viscous

particle deforms in a less viscous matrix, the shear-induced vorticity would be translated into components of shear induced spin of the particle and an addition of a coaxial component of flow inside the particle (Lister and Williams, 1983), resulting in particle rotation (spin) with respect to its matrix and deformation with an additional pure shear component (lower shear induced vorticity). The extent of this partitioning is dependent on the degree of decoupling of the particle–matrix interface and the viscosity ratio (e.g. Ishii, 1992; Schmid and Podladchikov, 2003). A difference of the vorticity number between a particle and its matrix (as a result of deformation partitioning) implies that the instantaneous stretching axes (ISA) inside the particle rotate with respect to the global reference frame (Lister and Williams, 1983). Modeling of the kinematics in multilayers as a function of layer orientation and viscosity contrast (Ishii, 1992; Jiang, 1994) when deforming by bulk simple shear, predicts a spin of the ISA within the more viscous layer with the sense of vorticity for synthetic layer orientations. With reference to our samples and assuming that quartz behaves as the higher viscous particle, this implies that the ISA inside the quartz aggregates change their orientation with respect to the matrix and that the flow type deviated from simple shear to a combination of simple and pure shear.

A rotation of the ISA out of a 45° fixed orientation (Fig. 16c) can explain the observed reverse shear senses, or the local persistence of a [c]-axis domain oriented for antithetic slip in the highly strained mylonite (Fig. 15) in the Gran Paradiso mylonites, i.e. the indicated in some quartz aggregates in the intermediately strained mylonite (Fig. 13). Basal <a> as the major slip system must be suitably oriented to accommodate microscopic shear (Fig. 16b and c). According to the [c]-axis maximum, many quartz basal planes in the recrystallized aggregates are inclined with respect to Xa such that slip in the observed sense is only reasonable if the orientation of the ISA is different for each deforming quartz aggregate and deviates from a fixed 45° orientation with respect to the shear zone boundary (Fig. 16c).

The inverse shear sense in the matrix–quartz aggregate interface and inside some aggregates (Fig. 13) during intermediate strain ($\varphi > 15°$) can be explained by the partitioning of flow between the quartz aggregates and the matrix. The ISA are expected to rotate with the aggregate – at least to some degree – , so the shear induced spin has to be compensated by flow parallel to the layer (- matrix interface) with the opposite sense of vorticity to the global flow. In other words, the bulk non-coaxial flow in the shear zone is discontinuous inside the quartz aggregates, and therefore the quartz aggregates spin, so that layer (aggregate) parallel shear must take place. Lister and Snoke (1984) observed similar effects on dikes dragged into a shear zone.

However, an alternative to flow partitioning to explain the quartz aggregate behavior and the contrasting shear senses is to assume that flow in the entire shear zone deviates strongly from simple shear plain strain. Menegon and Pennacchioni (2010) show that the shortening direction in the southern Gran Paradiso is at a high angle to the horizontal shear zones, based on the shear zone orientation distribution, shapes of mafic enclaves in the rock volumes between the shear zones and shapes of quartz aggregates inside mylonitic shear zones. However, the reversals of shear senses and differential deformation between quartz aggregates and matrix indicate that quartz aggregates do not behave as passive markers. Additionally it is uncertain whether the flow type inside the shear zone is identical to the flow type in the rock volumes between them. The shear zones must have a lower viscosity than the host rock and hence flow partitioning has to be expected, so that flow in the shear zone should at least have a higher shear induced vorticity than flow in the host rock (e.g. Jiang, 1994).

5.6. Implications for the interpretation of shear senses and microstructures

The microstructures and CPO development discussed above are typical for shear zones in the Gran Paradiso. They consist of more viscous quartz aggregates which deformed by dislocation creep in a less viscous matrix which deformed by diffusion creep at lower amphibolite facies conditions. In similar situations where flow partitioning may have occurred, shear sense interpretations based on shape fabrics and CPOs should be undertaken carefully.

We observe that the CPO has developed in a relationship to the quartz aggregate kinematic reference frame rather than to the global (shear zone) reference frame and also that opposite shear senses developed in aggregates oriented at small angles to the main shear zone. This situation may lead to erroneous interpretation of shear sense from orthorhombic [c]-axis pole figures if the kinematic reference frame is assumed to be fixed to the shear zone boundary and if the global reference frame is not known. This can be avoided if the highest strained parts of the shear zones are analyzed, because in these it is likely that quartz aggregates have reached a stable position with respect to the shear zone (parallel layering, high aspect ratio). Additionally, multiple measurements in different aggregates are recommended.

The surface ODF in the analyzed quartz aggregates are principally dependent on the CPO orientation. The active slip system is basal <a> which is fairly common at low to medium grade metamorphic conditions (Schmid and Casey, 1986; Takeshita, 1996; Stipp et al., 2002). If grain boundary mobility is low, a monoclinic surface ODF can be related to the sense of resolved microscopic shear. This sense of microscopic shear will not necessarily coincide with the global shear sense. A strong CPO and the resulting anisotropic distribution of the basal planes allow that slip can also be antithetic with respect to the macroscopic shear sense. An orthorhombic surface fabric appears to be indicative of higher grain boundary mobility and therefore only as reliable as the shear sense information obtained from the CPO.

6. Conclusions

The development of crystallographic preferred orientation of quartz has been studied in the Gran Paradiso metagranodiorite in small-scale shear zones, which formed at lower amphibolite facies conditions. Global and local reference frames have to be considered separately for the shear zone and for individual quartz aggregates.

1. Quartz aggregates deformed as more viscous particles in a weaker matrix, resulting in flow partitioning and a deviation of the local kinematic framework of quartz aggregates from the global kinematic framework of the shear zone.
2. Dynamic recrystallization resulted in a steady-state grain size and formation of CPO at relatively low strain.
3. The crystallographic orientation of the non-recrystallized magmatic quartz grains has had a minor influence on the final CPO. Even at low total strain, the initial CPO is usually related to the local kinematic framework.
4. The CPO maximum is synthetically inclined with the local shear sense and stable at ∼70° with respect to the local flow plane.
5. The orientation of a [c]-axis pole figure reflects the combination of the local kinematic framework, strain-dependent rotation of the CPO toward the stable position inside the aggregate, and rotation of the aggregates within the global reference frame.

6. Particle and surface fabrics are related to the [c]-axis orientation. Monoclinic surface fabrics indicate a shear sense consistent with the shear sense along an inferred basal <a> slip system but this may not necessarily be identical to the imposed global shear sense of the shear zone.

7. Development of monoclinic vs orthorhombic to symmetric fabrics is a function of the grain boundary velocity. Pinned grain boundaries are assumed to develop deformation controlled, monoclinic surface ODFs while more mobile grain boundaries tend to develop more symmetric surface ODFs controlled by other factors, e.g. crystallography.

8. Flow partitioning can explain a systematically opposite shear sense observed in aggregates inclined >15° with respect to the shear zone boundary.

9. We recommend that CPO and fabric measurements in rocks which have experienced flow partitioning (i.e. most polymineralic rocks) should only be performed in the most highly strained parts where aggregate rotation has largely ceased. Knowledge of the shear zone boundary orientation is indispensable.

Acknowledgments

References

Adams, B., 1993. Orientation imaging microscopy. Electron Microscopy and Analysis 1993 (138), 489–494.

Baeta, R., Ashbee, K., 1969. Slip systems in quartz: 2. Interpretation. American Mineralogist 54 (11–1), 1574–1582.

Behrmann, J., Platt, J., 1982. Sense of nappe emplacement from quartz c-axis fabrics – An example from the Betic cordilleras (Spain). Earth and Planetary Science Letters 59 (1), 208–215.

Berthe, D., Choukroune, S., Gapasi, D., 1979. Quartz fabrics and progressive gneissification of granites by simple shear – Example of the South Armorican shear zone. Bulletin De Mineralogie 102 (2–3), 265–272.

Bouchez, J., Duval, P., 1982. The fabric of polycrystalline ice deformed in simple shear – Experiments in torsion, natural deformation and geometrical interpretation. Textures and Microstructures 5 (3), 171–190.

Bouchez, J., 1977. Plastic-deformation of quartzites at low-temperature in an area of natural strain gradient. Tectonophysics 39 (1–3), 25–50.

Brouwer, F., Vissers, R., Lamb, W., 2002. Structure and metamorphism of the Gran Paradiso massif, Western Alps, Italy. Contributions to Mineralogy and Petrology 143 (4), 450–470.

Burg, J., Laurent, P., 1978. Strain analysis of a shear zone in a granodiorite. Tectonophysics 47 (1–2), 15–42.

Callegari, E., Compagnoni, R., Piaz, G.D., 1969. Relitti di strutture intrusive erciniche e scisti a sillimanie nel Massicio del Gran Paradiso. Bollettino della Società geologica italiana 88, 59–69.

Carreras, J., Estrada, A., White, S., 1977. Effects of folding on c-axis fabrics of a quartz mylonite. Tectonophysics 39 (1–3), 3–24.

Dal Piaz, G., Hunziker, J., Martinotti, G., 1972. La zona Sesia-Lanzo e l'evoluzione tettonico-metamorfica delle Alpi nordoccidentali interne. Memoir Societa Geologica Italiana 11, 433–466.

DellAngelo, L., Tullis, J., 1989. Fabric development in experimentally sheared quartzites. Tectonophysics 169 (1–3), 1–21.

Drury, M., Urai, J., 1990. Deformation-related recrystallization processes. Tectonophysics 172 (3–4), 235–253.

Etchecopar, A., Vasseur, G., 1987. A 3-d kinematic model of fabric development in polycrystalline aggregates – Comparisons with experimental and natural examples. Journal of Structural Geology 9 (5–6), 705–717.

Etchecopar, A., 1977. Plane kinematic model of progressive deformation in a polycrystalline aggregate. Tectonophysics 39 (1–3), 121–139.

Freeman, B., 1987. The behavior of deformable ellipsoidal particles in 3-dimensional slow flows – Implications for geological strain analysis. Tectonophysics 132 (4), 297–309.

Garcia-Celma, A., 1983. c-axis and shape fabrics in quartz-mylonites of Cap de Creus (Spain); their properties and development. Ph.D. thesis, University of Utrecht.

Guillope, M., Poirier, J., 1980. Model for stress-induced migration of tilt grain-boundaries in crystals of NaCl structure. Acta Metallurgica 28 (2), 163–167.

Heilbronner, R., Bruhn, D., 1998. The influence of three-dimensional grain size distributions on the rheology of polyphase rocks. Journal of Structural Geology 20 (6), 695–705.

Heilbronner, R., Pauli, C., 1993. Integrated spatial and orientation analysis of quartz c-axes by computer-aided microscopy. Journal of Structural Geology 15 (3–5), 369–382.

Heilbronner, R., Tullis, J., 2006. Evolution of c axis pole figures and grain size during dynamic recrystallization: results from experimentally sheared quartzite. Journal of Geophysical Research-Solid Earth 111 (B10), B10202.

Heilbronner, R., 2000. Automatic grain boundary detection and grain size analysis using polarization micrographs or orientation images. Journal of Structural Geology 22 (7), 969–981.

Heilbronner, R., 2002. Analysis of bulk fabrics and microstructure variations using tessellations of autocorrelation functions. Computers and Geosciences 28 (4), 447–455.

Hielscher, R., Schaeben, H., 2008. A novel pole figure inversion method: specification of the MTEX algorithm. Journal of Applied Crystallography 41, 1024–1037.

Hudleston, P., 1980. The progressive development of inhomogeneous shear and crystallographic fabric in glacial ice. Journal of Structural Geology 2 (1–2), 189–196.

Ishii, K., 1992. Partitioning of noncoaxiality in deforming layered rock masses. Tectonophysics 210 (1–2), 33–43.

Jerabek, P., Stuenitz, H., Heilbronner, R., Lexa, O., Schulmann, K., 2007. Microstructural-deformation record of an orogen-parallel extension in the Vepor unit, West Carpathians. Journal of Structural Geology 29 (11), 1722–1743.

Jessell, M., Lister, G., 1990. A Simulation of Temperature Dependence of Quartz Fabrics. In: Geological Society of London Special Publication, vol. 54, pp. 353–362.

Jiang, D., 1994. Flow variation in layered rocks subjected to bulk flow of various kinematics vorticities – Theory and geological implications. Journal of Structural Geology 16 (8), 1159–1172.

Kassem, O., 2005. Finite-Strain analysis in Orthogneiss of the Gran Paradiso massif, Western Alps, Italy. Ph.D. thesis, University Mainz.

Kilian, R., Heilbronner, R., Stünitz, H., 2011. Quartz grain size reduction in a granitoid rock and the transition from dislocation to diffusion creep. Journal of Structural Geology 33 (8), 1265–1284.

Knipe, R., Law, R., 1987. The influence of crystallographic orientation and grain-boundary migration on microstructural and textural evolution in an s-c mylonite. Tectonophysics 135 (1–3), 155–169.

Kruhl, J., Peternell, M., 2002. The equilibration of high-angle grain boundaries in dynamically recrystallized quartz: the effect of crystallography and temperature. Journal of Structural Geology 24 (6–7), 1125–1137.

Kuntcheva, B., Kruhl, J.H., Kunze, K., 2006. Crystallographic orientations of high-angle grain boundaries in dynamically recrystallized quartz: first results. Tectonophysics 421 (3–4), 331–346.

Law, R., Schmid, S., Wheeler, J., 1990. Simple shear deformation and quartz crystallographic fabrics – A possible natural example from the Torridon area of NW Scotland. Journal of Structural Geology 12 (1), 29–45.

Law, R., 1986. Relationships between strain and quartz crystallographic fabrics in the Roche Maurice Quartzites of Plougastel, Western Brittany. Journal of Structural Geology 8 (5), 493–515.

Le Bayon, B., Pitra, P., Ballevre, M., Bohn, M., 2006. Reconstructing P-T paths during continental collision using multi-stage garnet (Gran Paradiso nappe, Western Alps). Journal of Metamorphic Geology 24 (6), 477–496.

LeGoff, E., Ballevre, M., 1990. Geothermobarometry in albite-garnet orthogneisses – A case-study from the Gran-Paradiso nappe (Western Alps). Lithos 25 (4), 261–280.

Lister, G., Hobbs, B., 1980. The simulation of fabric development during plastic-deformation and its application to quartzite – The influence of deformation history. Journal of Structural Geology 2 (3), 355–370.

Lister, G., Snoke, A., 1984. s-c mylonites. Journal of Structural Geology 6 (6), 617–638.

Lister, G., Williams, P., 1979. Fabric development in shear zones – Theoretical controls and observed phenomena. Journal of Structural Geology 1 (4), 283–297.

Lister, G., Williams, P., 1983. The partitioning of deformation in flowing rock masses. Tectonophysics 92 (1–3), 1–33.

Lister, G., Paterson, M., Hobbs, B., 1978. Simulation of fabric development in plastic-deformation and its application to quartzite – Model. Tectonophysics 45 (2–3), 107–158.

Mancktelow, N., 1987. Quartz textures from the Simplon fault zone, southwest Switzerland and north Italy. Tectonophysics 135 (1–3), 133–153.

Marques, F., Taborda, R., Antunes, J., 2005. 2d rotation of rigid inclusions in confined bulk simple shear flow: a numerical study. Journal of Structural Geology 27 (12), 2171–2180.

Means, W., 1981. The concept of steady-state foliation. Tectonophysics 78 (1–4), 179–199.

Menegon, L., Pennacchioni, G., 2010. Local shear zone pattern and bulk deformation in the Gran Paradiso metagranite (NW Italian Alps). International Journal of Earth Sciences 99, 1805–1825.

Menegon, L., Pennacchioni, G., Stuenitz, H., 2006. Nucleation and growth of myrmekite during ductile shear deformation in metagranites. Journal of Metamorphic Geology 24 (7), 553–568.

Menegon, L., Pennacchioni, G., Spiess, R., 2008. Dissolution-precipitation creep of K-feldspar in mid-crustal granite mylonites. Journal of Structural Geology 30 (5), 565–579.

Mulchrone, K., Walsh, K., 2006. The motion of a non-rigid ellipse in a general 2D deformation. Journal of Structural Geology 28 (3), 392–407.

Mulchrone, K.F., 2007. An analytical solution in 2D for the motion of rigid elliptical particles with a slipping interface under a general deformation. Journal of Structural Geology 29 (6), 950–960.

Olgaard, D., Evans, B., 1986. Effect of 2nd-phase particles on grain-growth in calcite. Journal of the American Ceramic Society 69 (11), C272–C277.

Panozzo, R., 1983. Two-dimensional analysis of shape-fabric using projections of digitized lines in a plane. Tectonophysics 95 (3–4), 279–294.

Panozzo, R., 1984. Two-dimensional strain from the orientation of lines in a plane. Journal of Structural Geology 6 (1–2), 215–221.

Passchier, C.W., Trouw, R.A.J., 1996. Microtectonics. Springer Verlag, Berlin.

Passchier, C.W., 1983. The reliability of asymmetric c-axis fabrics of quartz to determine sense of vorticity. Tectonophysics 99 (1), T9–T18.

Passchier, C.W., 1987. Stable positions of rigid objects in noncoaxial flow – A study in vorticity analysis. Journal of Structural Geology 9 (5–6), 679.

Pauli, C., Schmid, S., Heilbronner, R., 1996. Fabric domains in quartz mylonites: localized three dimensional analysis of microstructure and texture. Journal of Structural Geology 18 (10), 1183–1203.

Pennacchioni, G., Menegon, L., Leiss, B., Nestola, F., Bromiley, G., 2010. Development of crystallographic preferred orientation and microstructure during plastic deformation of natural coarse-grained quartz veins. Journal of Geophysical Research-Solid Earth 115.

Platt, J.P., Behr, W.M., 2011. Grainsize evolution in ductile shear zones: implications for strain localization and the strength of the lithosphere. Journal of Structural Geology 33 (4), 537–550.

Poirier, J., Guillope, M., 1979. Deformation induced recrystallization of minerals. Bulletin De Mineralogie 102 (2–3), 67–74.

Ramsay, J.F., Huber, M.I., 1983. The Techniques of Modern Structural Geology. Academic Press, London.

van Roermund, H., Lister, G., Williams, P., 1979. Progressive development of quartz fabrics in a shear zone from Monte-Mucrone, Sesia-Lanzo-Zone, Italian Alps. Journal of Structural Geology 1 (1), 43–52.

Schmid, S., Casey, M., 1986. Complete Fabric Analysis of Some Commonly Observed Quartz c-axis Patterns. In: Geophysical Monograph, vol. 36. American Geophysical Union, pp. 263–286.

Schmid, D., Podladchikov, Y., 2003. Analytical solutions for deformable elliptical inclusions in general shear. Geophysical Journal International 155 (1), 269–288.

Schmid, S., Panozzo, R., Bauer, S., 1987. Simple shear experiments on calcite rocks – Rheology and microfabric. Journal of Structural Geology 9 (5–6), 747–778.

Schmid, S., 1994. Textures of Geological Materials: Computer Model Predictions Versus Empirical Interpretations Based on Rock Deformation Experiments and Field Studies. DGM, Informationsgesellschaft, pp. 279–301.

Shigematsu, N., Prior, D.J., Wheeler, J., 2006. First combined electron backscatter diffraction and transmission electron microscopy study of grain boundary structure of deformed quartzite. Journal of Microscopy 224, 306–321.

Simpson, C., Schmid, S., 1983. An evaluation of criteria to deduce the sense of movement in sheared rocks. Geological Society of America Bulletin 94 (11), 1281–1288.

Simpson, C., 1980. Oblique girdle orientation patterns of quartz c-axes from a shear zone in the basement core of the Maggia-Nappe, Ticino, Switzerland. Journal of Structural Geology 2 (1–2), 243–247.

Stipp, M., Stunitz, H., Heilbronner, R., Schmid, S., 2002. The eastern Tonale Fault Zone: a 'natural laboratory' for crystal plastic deformation of quartz over a temperature range from 250 to 700 °C. Journal of Structural Geology 24 (12), 1861–1884.

Stunitz, H., 1991. Folding and shear deformation in quartzites, inferred from crystallographic preferred orientation and shape fabrics. Journal of Structural Geology 13 (1), 71–86.

Takeshita, T., 1996. Estimate of physical conditions for deformation based on c-axis transitions in naturally deformed quartzite. Journal of the Geological Society of Japan 102 (3), 211–222.

Trepied, L., Doukhan, J., Paquet, J., 1980. Subgrain boundaries in quartz – Theoretical-analysis and microscopic observations. Physics and Chemistry of Minerals 5 (3), 201–218.

Tullis, J., 1977. Preferred orientation of quartz produced by slip during plane strain. Tectonophysics 39 (1–3), 87–102.

Wenk, H., Canova, G., Molinari, A., Kocks, U., 1989. Viscoplastic modeling of texture development in quartzite. Journal of Geophysical Research-Solid Earth and Planets 94 (B12), 17895–17906.

White, S., 1976. The Role of Dislocation Processes during Tectonic Deformation with Special Reference to Quartz. In: The Physics and Chemistry of Minerals and Rocks. Wiley, London, pp. 75–91.